PHYSICAL REVIEW APPLIED **22,** 044022 (2024)

# Terahertz emission from mutually synchronized standalone $Bi_2Sr_2CaCu_2O_{8+x}$ intrinsic-Josephson-junction stacks

Raphael Wieland,[1,*] Olcay Kizilaslan,[1,2] Nickolay Kinev,[3] Eric Dorsch,[1] Stefan Guénon,[1]
Ziyu Song,[4] Zihan Wei,[5] Huabing Wang,[4,5] Peiheng Wu,[4,5] Dieter Koelle,[1] Valery P. Koshelets,[3]
and Reinhold Kleiner[1,†]

[1] *Physikalisches Institut, Center for Quantum Science and LISA*$^+$, *Universität Tübingen, 72076 Tübingen, Germany*
[2] *Department of Biomedical Engineering, Faculty of Engineering, Inonu University, Malatya, Turkey*
[3] *Kotel'nikov Institute of Radio Engineering and Electronics, Moscow, 125009, Russia*
[4] *Research Institute of Superconductor Electronics, Nanjing University, Nanjing, 210023, China*
[5] *Purple Mountain Laboratories, Nanjing, 211111, China*

(Received 30 April 2024; revised 23 July 2024; accepted 12 September 2024; published 9 October 2024)

Suitably patterned single crystals made of the cuprate superconductor $Bi_2Sr_2CaCu_2O_{8+x}$ (BSCCO), intrinsically forming a stack of Josephson junctions, can generate electromagnetic radiation in the lower terahertz regime. Because of Joule heating, the emission power of single stacks seems to be limited to values below 100 μW. To increase the radiation power, mutually synchronized arrays situated on the same BSCCO base crystal have been studied. A maximum power of almost 1 mW has been achieved by synchronization of three stacks. Mutual electromagnetic interactions via a connecting BSCCO base crystal have been considered essential for synchronization, but the approach still suffers from Joule heating, preventing the synchronization of more than three stacks. In the present paper we show, on the basis of two emitting stacks, that mutual synchronization can also be achieved by standalone stacks contacted by gold layers and sharing only a common gold layer. Compared with BSCCO base crystals, the gold layers have a much higher thermal conductivity and their patterning is not very problematic. We analyze our results in detail, showing that the two oscillators exhibit phase correlations over a range of ±0.4 GHz relative to their center frequencies, which we studied mainly between 745 and 765 GHz. However, we also find that strong phase gradients in the beams radiated from both the mutually locked stacks and the unlocked stacks play an important role and, presumably, diminish the detected emission power due to destructive interference. We speculate that the effect arises from higher-order cavity modes that are excited in the individual stacks. Our main message is that the mutual interaction provided by a common gold layer may open new possibilities for relaxing the Joule-heating problem, allowing the synchronization of a higher number of stacks. The approach may also allow one to synchronize several stacks that are comparatively small in size and less prone to the strong phase gradients we observed. Our findings may boost attempts to substantially increase the output power levels of BSCCO terahertz oscillators.

DOI: 10.1103/PhysRevApplied.22.044022

## I. INTRODUCTION

The cuprate superconductor $Bi_2Sr_2CaCu_2O_{8+x}$ (BSCCO), once properly patterned, is known to emit electromagnetic radiation in the range from 0.2 THz up to a few terahertz. This frequency regime is highly interesting for applications but only sparsely populated with compact solid-state sources [1–4]. BSCCO is a layered superconductor with alternating superconducting and insulating sheets. A single crystal thus forms a natural stack of intrinsic Josephson junctions (IJJs), with approximately 670 junctions per micrometer of crystal thickness [5]. In the resistive state, the supercurrents across each IJJ oscillate with frequency $f_J = V_J/\Phi_0$, where $V_J$ is the voltage across the junction and $\Phi_0$ is the flux quantum, $\Phi_0^{-1} = 483.6$ GHz/mV. Provided that the IJJs can be phase-synchronized, such a stack can act as a voltage-tunable emitter of coherent electromagnetic waves. BSCCO emitters have attracted great interest in recent years, both experimentally [6–51] and theoretically [52–76]. For recent reviews, see Refs. [77–81]. Coherent off-chip terahertz emission in the frequency range between 0.5 and 0.85 THz was first reported for rectangular and 1-μm-thick mesas patterned on a BSCCO base crystal, with an extrapolated output power of up to 0.5 μW [6]. The mesas were about

---

[*] Contact author: raphael.wieland@uni-tuebingen.de
[†] Contact author: kleiner@uni-tuebingen.de

300 μm long and several tens of micrometers wide. The emission frequency was found to be inversely proportional to the width of the stack, leading to the conclusion that resonant cavity modes oscillating along the width of the stack play an important role in synchronizing the junctions in the stack. Later, a variety of cavity resonances were found and analyzed [7,8,10,11,33,37,39,40,48,53,57,58,69].

In addition to the mesa-type structures, IJJ stacks have also been realized as standalone structures, where the BSCCO stack is contacted by gold layers from both sides, and sometimes also as $z$-type structures, where the stack and contacting electrodes were patterned from a solid BSCCO single crystal [30,80]. It further turned out for all structures that Joule heating plays an important role and for a large input power leads to the formation of a hot spot, a region within the stack with a temperature above the critical temperature $T_c$ [7,10,17,19,21,59,63]. The hot spot can coexist with regions that are still superconducting and produce terahertz radiation. Joule heating is also reflected in the shape of the current-voltage characteristic (IVC) of the stack. For low bias currents, the input power is moderate and the temperature distribution in the stack is almost homogeneous and close to the bath temperature $T_{\mathrm{bath}}$. In this “low-bias regime” the IVCs exhibit a positive differential resistance. With increasing current, because the out-of-plane resistivity of BSCCO decreases with increasing temperature, the IVCs start to back-bend, and above some threshold current the hot spot forms and increases in size with increasing current and input power (“high-bias regime”). Joule heating and the presence of a hot spot affect radiation. On the one hand, it is found that the linewidth of radiation is much lower in the presence of the hot spot [16], and in addition the emission frequency becomes tunable by manipulation of the hot spot’s size and position [25–27]. On the other hand, Joule heating limits the maximum voltage across the junctions and thus the maximum emission frequency. Joule heating also limits the total number of junctions $N$ in the stack and thus the maximum emission output power, which ideally should scale in proportion to $N^2$. Thermal management thus became an issue over the years. Originally, the IJJ stacks were realized as mesa structures patterned on BSCCO single crystals that were just glued with epoxy resin to a cooled substrate [6]. To improve cooling, the crystals have for example, been soldered to Cu substrates [31], and double-sided cooling techniques have been applied to standalone stacks [23,24,28,29]. In this way, output powers of several tens of microwatts have been achieved. The maximum emission frequencies increased to 2.4 THz and $N$ increased to around 3000.

Even after improvements, the maximum emission frequencies seem to be limited to values below 2.5 THz and the maximum emission power seems to be limited to values below 100 μW for the large structures described above. In terms of emission frequencies, substantially higher values of up to 11 THz have been obtained by the use of stacks with much smaller in-plane dimensions of around 10 μm consisting of only around 200 IJJs [36]. The radiation-power efficiency for the typically used IJJ stacks is presently well below 1%, perhaps with one exception [44]. To increase this efficiency, the use of properly designed antenna structures [38,45–47,62,72–74,82], or the use of resonators [43] has been proposed and partially realized.

The third approach, which can presumably be combined with the former ones, is to mutually phase-lock planar arrays of stacks located on the same chip, like for arrays of conventional Josephson junctions [83–88]. The present paper intends to contribute to this approach. Criteria to distinguish locked states from unlocked ones include the narrowing of the linewidth of radiation, the increase of the emitted radiation power, the comparison of the dc voltages across the stacks, and the change in the angular dependence of the polarization of the emitted-radiation patterns. Presently, the amount of literature on coupled IJJ stacks is modest [12,20,30,42,64,65,75,76,89]. In Ref. [30], the mutual interaction of two $z$-type structures was investigated, but no clear signatures of mutual phase-locking were found. References [12,20,42,64,75,76] considered mesa-type structures. Clear evidence for mutual phase-locking was given in these pioneering studies, and it was concluded that the common base crystal is required to provide an electromagnetic interaction via Josephson plasma waves propagating in the base crystal. In particular, Ref. [20] reported an output power of up to 0.63 mW for an emission frequency of 0.51 THz for synchronization of three adjacent mesas, with a spacing of 60 μm between the mesas. The main obstacle to mutually synchronize more stacks is still Joule heating, which is reinforced by the poor thermal conductance of the BSCCO base crystal but, on the other hand, seems to be necessary for mutual coupling. Below, we report on the synchronization of two standalone stacks that share a common Au base electrode, with a spacing between the stacks of 200 μm. The data show that a common base crystal and thus an interaction via Josephson plasma waves is not required for mutual electric coupling. In the present experiment, the stacks including the gold layer were mounted on the sample holder with the use of epoxy resin, as in the experiments performed with mesas. Consequently, the effect of self-heating is still strong. Throughout this paper, we analyze this geometry to describe our data. However, an important message is that the common gold electrode could be made thicker and brought into a thermally-well-conductive metallic contact to a thermally anchored substrate. Such a revised geometry could relax the notorious heating problem to synchronize a larger number of stacks.

## II. SAMPLES AND EXPERIMENTAL TECHNIQUES

The sample investigated is patterned from a slightly underdoped BSCCO single crystal, with $T_c$ of 86 K. The stacks are realized as gold-BSCCO-gold structures, with the use of a procedure similar to the one described in Ref. [23]. In brief, a thin flake of the crystal is glued with epoxy resin onto a 1-mm-thick sapphire substrate. The upper layers are removed with the use of adhesive tape and the new crystal surface is covered by about 200 nm of gold (thermal evaporation). With the use of optical lithography and argon-ion etching, five rectangular mesas are patterned onto the gold-covered BSCCO. Another sapphire substrate is glued onto them, and then the first substrate is removed, cleaving off the common base crystal. Another gold layer with a thickness of 70 nm is evaporated onto the fresh BSCCO surface.

By optical lithography, followed by ion etching, the width of this film is reduced to 300 μm along the long side of the IJJ stacks, the latter protruding about 150 μm on both sides from the gold. These parts are etched down until the lower gold layer is accessible. The remaining parts of the lower gold layer are used to individually make electrical contact to the stacks, while the upper, 70-nm-thick gold layer, still stretching across all stacks, is used as common ground. A sketch of the completely fabricated sample is shown in Figs. 1(a) and 1(b). The sample includes five stacks in total. For the experiments, we used only stacks a and b, located on the left of the sketches. An optical image of these stacks is shown in Fig. 1(c). The contacts to the neighboring stack c had a short, while stacks d and e had reasonably looking IVCs but exhibited only an extremely small emission power that could not be evaluated further. A readjustment of the optical path (after the lens) did not lead to an increase of the emission power of stacks d and e; thus, we must conclude that the emission from these stacks is indeed poor. Thus, emission and synchronization experiments were feasible only for stacks a and b. The stacks' dimensions are approximately $50 \times 300 \times 0.7$ μm$^3$, and the number of junctions per stack $N \approx 460$, as determined from emission measurements. The gap between the stacks is 200 μm in width.

For the described sample design, each stack has two BSCCO-gold interfaces, one on the top side and one on the bottom side, allowing a two-terminal scheme for measurements of the IVC of each stack, which includes the contact resistances between BSCCO and the gold layers. For emission measurements, the sample is mounted on a hemispheric sapphire lens, as sketched in Figs. 1(a) and 1(b).

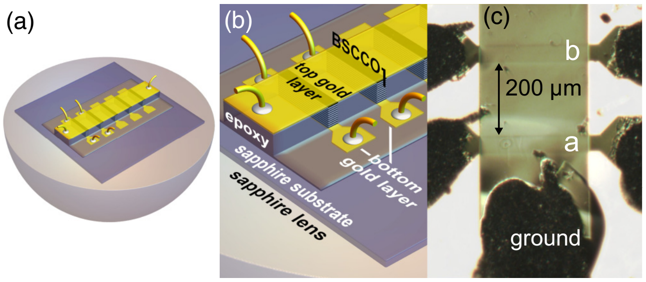

FIG. 1. Sample geometry. (a),(b) Sample mounted on a hemispheric lens. (c) Optical image of stacks a and b used for synchronization experiments. The fabrication steps to obtain this structure are described briefly in the main text and in more detail in Ref. [23].

The sample was precharacterized by transport and emission experiments with use of a niobium-based superconducting integrated receiver (SIR) as a detector for the emitted radiation, providing evidence that the two stacks can be phase-locked. Some results and details of the setup are reported in Ref. [89]. In brief, the setup includes two optical helium-bath cryostats, one hosting the emitter and the other hosting the detector. The incoming signal at frequency $f_s$ is mixed with the reference signal of a superconducting Josephson-junction local oscillator at frequency $f_{LO}$ to yield a difference (intermediate) frequency $f_{IF}$ that is analyzed conventionally in subsequent steps [90]. The frequency resolution of this heterodyne detection scheme is better than 1 MHz and is required to resolve the linewidth of radiation of the BSCCO emitter. With the local oscillator fixed at 650 GHz and the unregulated sample holder kept at 14 K, phase synchronization of the two stacks was observed when the bias current of one of the stacks was varied while the bias current through the other stack was kept fixed. Figure 2 shows some additional results. The three curves displayed are for three different bias currents through stack b while the current through stack a remained constant. In the unlocked regime, two emission lines with individual linewidths of around 35–40 MHz were visible. In the locked regime, the two lines collapsed to a single line with an emission frequency near 644 GHz and a linewidth of about 24 MHz. Also, the integrated emission power exceeded the sum of the individual emission powers by 15–20%. Of further note, the emission line through stack a also changes its frequency. This is because the (varying) Joule heating in stack b also causes a temperature change and thus a change in, respectively, voltage and emission frequency in stack a. After 2021, we continued our study of mutual synchronization using the setup shown schematically in Fig. 3. Here we have much less frequency resolution that in the SIR setup but it is possible to cover a wider range of emission frequencies. Also, with more data points measured, it is easier to distinguish between power modulations of the individual stacks and and power changes due to mutual synchronization.

For the experiments described below we used the same sample and stacks as in the heterodyne mixing experiment. This sample is mounted near but not exactly in the focus of the hemispheric lens. The wiring from the sample through

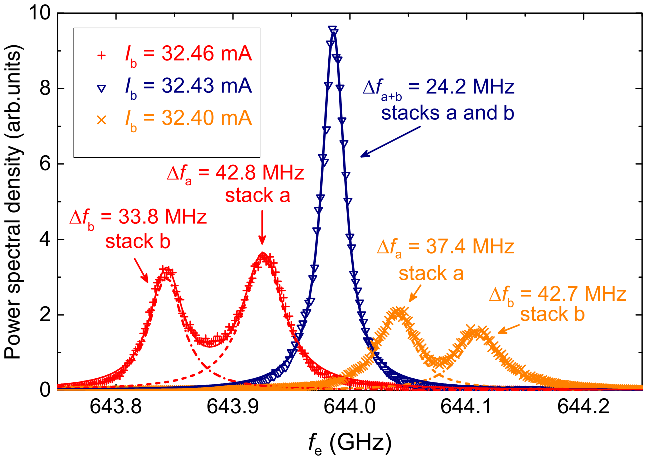

FIG. 2. Selected emission data obtained with the SIR. Power spectral density for three different current values of stack b. The current through stack a remained constant, $I_a = 24.24$ mA. Data for different bias currents through stack b are distinguished by different colors and symbols: 32.46 mA (+), 32.43 mA ($\nabla$), and 32.40 mA ($\times$). Data are fitted by Lorentzians, given in the same colors. Two Lorentzians have been used for, respectively, $I_b = 32.46$ mA and $I_b = 32.40$ mA. Individual contributions are indicated by dashed lines; their sum is plotted as solid lines. A single Lorentzian has been used for $I_b = 32.43$ mA. The extracted linewidths of radiation are indicated. $\Delta f_{(a+b)}$ denotes the linewidth of radiation in the synchronized case.

the cryostat is done with separate wires for current and voltage (for the top contact of stack b, only one wire, due to a broken bond). After having passed the lens, the beams emitted by the stacks have presumably widened to the millimeter scale. As shown previously [33], the intensity of radiation emitted by one stack after the lens is strongly peaked in the forward direction, with a divergence of around ±5°. Since the position of the two stacks is somewhat out of the focal point of the lens, the two radiation beams are likely to be directed slightly away from the optical axis. Next, the emission fields are directed through the high-density-polyethylene window of the optical He-flow cryostat and pass the plane of the chopper, which periodically opens and closes with frequency $\omega_{ch} = 2\pi \times 80$ Hz. The chopper is located at a distance of approximately 6 cm from the lens. In the plane of the chopper, the beams emitted by the two stacks have widened to a diameter of around 2 cm and will partially overlap. After the chopper, the beams are first reflected by a 90° parabolic mirror (M1) and then by a planar mirror (M2), followed by a second 90° parabolic mirror (M3) that focuses the beams into the entrance of the Winston cone located in a He-bath cryostat. The Winston cone guides the signal, through several reflections, to the Ge bolometer mounted on the exit side of the Winston cone. The bolometer detects the signal incoherently. Finally, the signal created by the bolometer, which is periodically modulated in time by the chopper, is multiplied by the reference signal of a vector lock-in amplifier and integrated over time. Below, for an in-phase multiplication of the reference phase by the signal, the output is called "channel X," while for an out-of-phase multiplication it is called "channel Y." The lock-in amplifier is set to record the bolometer signal dominantly in channel X and for a smaller part in channel Y.

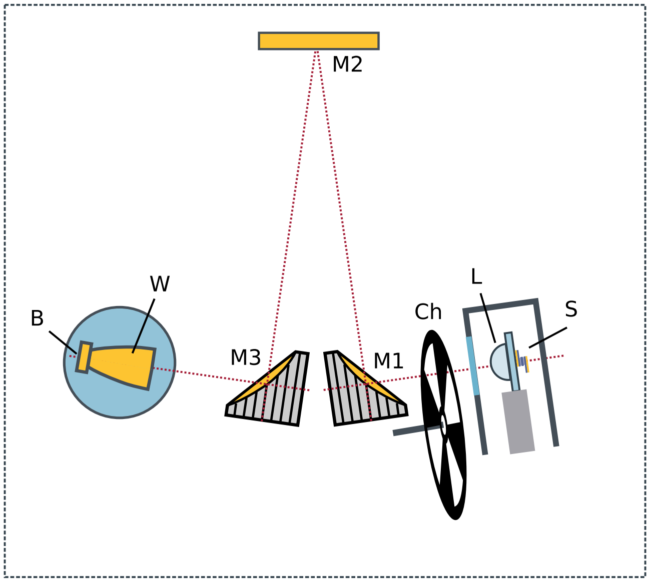

FIG. 3. Geometry of the experiment. The sample (S) is mounted on a hemispheric lens (L). The emitted light fields propagate (roughly) along the optical path indicated by the dotted line. Having left the cryostat, the light fields are modulated by the chopper (Ch), are reflected by the first parabolic mirror (M1), and then pass the planar mirror (M2) and the second parabolic mirror (M3). They are subsequently collected by the Winston cone (W) and are directed to the bolometer (B), which produces a time-modulated intensity that is subsequently processed by a vector lock-in amplifier.

The flat mirror M2 can be replaced by a homemade lamellar split mirror for Fourier spectroscopy, with a frequency resolution of about 10 GHz [13]. This interferometer can be used for a first but not-very-precise determination of the emission frequency.

Usually, the whole interferometer setup is flooded with nitrogen gas to reduce water-vapor absorption. However, in some experiments discussed below we flood the setup with ambient air and use the water-vapor absorption line at $f_{water} \approx 752.033$ GHz for frequency calibration. This is necessary for a precise comparison of the emission frequency of the two stacks.

## III. RESULTS

As a precharacterization, the inset in Fig. 4(a) shows the resistance of stack a versus bath temperature $T_{bath}$. The resistive transition occurs at $T_c \approx 86$ K, and the overall shape of $R_a$ versus $T_{bath}$ indicates that the sample is slightly underdoped [91]. The main panel in Fig. 4(a) shows the

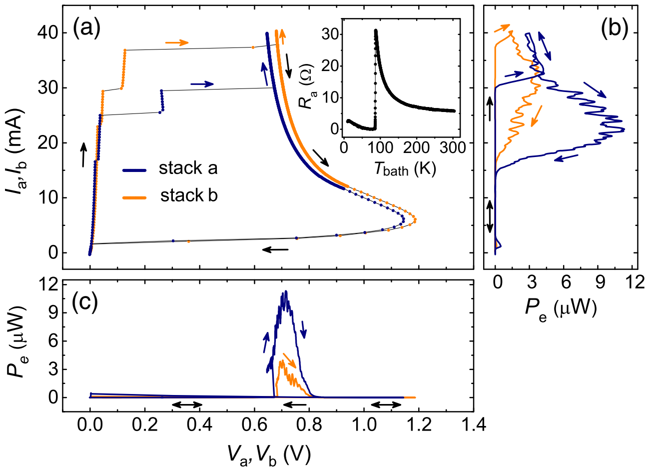

FIG. 4. (a) IVCs of stacks a and b, biased only one at a time, at $T_{\text{bath}} = 10$ K. For stack b, an Ohmic resistance of 2.3 Ω has been subtracted from the data to remove the parasitic contribution from the wire connecting the sample to the room-temperature part of the setup. The inset shows resistance versus bath temperature for stack a. (b),(c) Emission power, as detected by the bolometer, as a function of (b) bias current and (c) voltage across the stacks. Emission measurements were done simultaneously with the corresponding IVC measurement. In all graphs, arrows indicate the direction of the current sweeps. Different colors are used to distinguish stack a and stack b.

IVCs of the two stacks at $T_{\text{bath}} = 10$ K. The stacks were biased only one at a time. For each stack, the current is increased from 0 to 40 mA and subsequently reduced back to zero. The voltage appears as measured, i.e., contact resistances are included. Note that the measured resistance of stack b contains an additional contribution of 2.3 Ω from the wire leading out of the cryostat. We corrected for this contribution before showing the data in Fig. 4. One observes the typical hysteretic IVCs of IJJ stacks, where upon increase of the current, groups of IJJs successively become resistive. For $I_a > 30$ mA ($I_b > 37$ mA) all IJJs within stack a (stack b) are resistive and remain in this state until the current is reduced to values below 2 mA. Figures 4(b) and 4(c) show the emitted power as a function of, respectively, current and voltage, as detected by the bolometer while recording the IVCs. For both stacks, emission occurred mainly in the high-bias regime, where a hot spot has formed inside the stacks. Maximum-emission-power readings were around 10 μW for stack a and 4 μW for stack b. For both stacks the switch from the zero-voltage state to the fully resistive state cuts off the emission on the low-voltage side, as indicated by the arrows showing the sweep direction.

Further note that the bolometer readings for both stacks show oscillations both as a function of current and as a function of voltage. This translates into a modulated emission power as a function of emission frequency, where the quasiperiodic oscillations occur on a frequency scale of around 3 GHz up to some 10 GHz. Many published data show this effect [22,26,66,67,76]. The modulations could, in principle, arise from the excitation of different cavity modes in the stack. The effect is well known and has been analyzed extensively in the literature; see, e.g., Refs. [33,48]. However, the resonance frequencies of different cavity modes are separated by tens of gigahertz, and there are simply not enough cavity resonances to explain the numerous oscillations we observe. In addition, we tried to correlate the linewidth of radiation, as measured by the SIR, with the few-gigahertz modulations. The result was negative—we could not see a clear correlation. Thus, we conclude that these oscillations are due to interference that occurs outside the stacks. We assume that the beam emitted by a single stack has a smooth phase profile in the radial direction after having passed the lens. The different radial parts of the beam may have traveled a different path difference $\Delta l$ before the detection by the bolometer. Then one would expect a phase difference of $2\pi$ between the two paths for a frequency difference $\Delta f$ on the order of $c/\Delta l$, yielding $\Delta l = 10$ cm for $\Delta f = 3$ GHz. This value is far too large to be explainable by inaccuracies in our detection scheme, e.g., by geometric aberrations caused by the parabolic mirrors [92] or by multiple reflections in the Winston cone. We have also ruled out that the cryostat windows or reflections inside the cryostat are the origin of the modulations. A remaining possibility arises from the fact that for a given cavity mode the Josephson phase along the edges of the stack can vary strongly. Below we give arguments that a $(1, 3)$ cavity mode was excited in our experiments. Here, the resonance pattern forms one half-wave along the width and three half-waves along the length of the stack, and thus the phase gradients amount to $3\pi$ along the length and $\pi$ along the width. The lens may heavily mix the corresponding wave fronts. This may also change the directivity of the emitted radiation when the emission frequency is varied. Whether this effect can explain the observed oscillations is unclear. We thus need to treat the origin of the power oscillations and the phase profiles of the emitted-radiation beams as an unknown when analyzing the interference of the light fields created by the two oscillators.

In the experiments discussed next, we perform a broadband measurement of the combined emission power of both stacks while varying their bias currents $I_a$ and $I_b$ over some range.

The result is shown in Fig. 5(a) for lock-in channel X. One notes oscillations of the detected power slightly tilted from the vertical and horizontal directions, plus a strongly tilted "diagonal" line. The slightly tilted lines resembling a Scottish tartan arise from the power modulations of the individual stacks, as already visible in Fig. 4(b). In general, we may write the total detected power as

$$P_{\text{tot},\alpha}(I_a, I_b) = P_{a,\alpha}(I_a) + P_{b,\alpha}(I_b) + P_{ab,\alpha}(I_a, I_b). \quad (1)$$

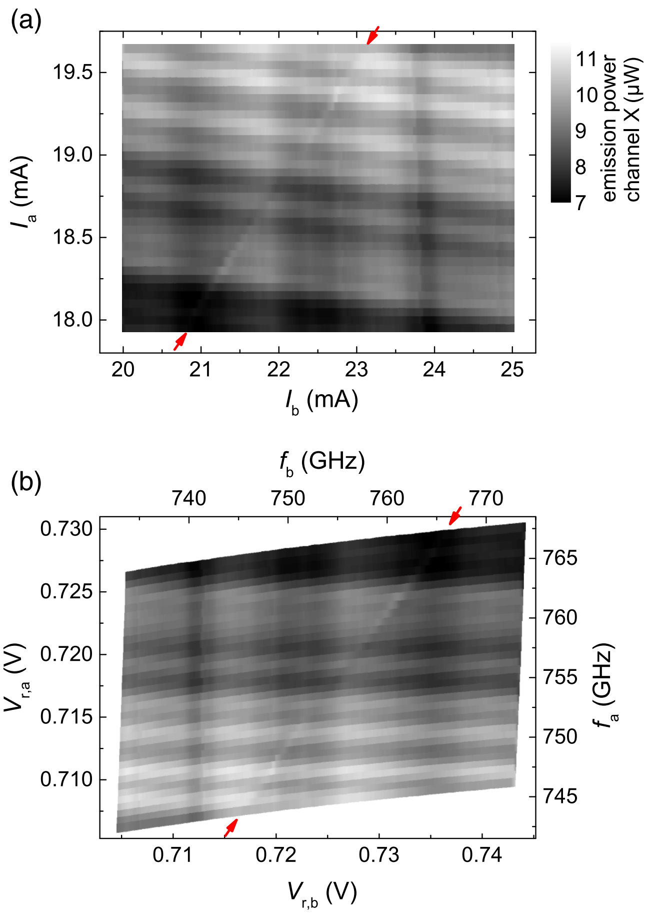

FIG. 5. For lock-in channel X: emission data for the two stacks biased at the same time. (a) Bolometric power as a gray scale plotted against stack currents $I_a$ and $I_b$. (b) Bolometric data as a function of the rescaled voltages $V_{r,a}$ and $V_{r,b}$ (left and bottom axes) and the corresponding emission frequencies $f_a$ and $f_b$ (right and top axes). For determination of $V_{r,a}$ and $V_{r,b}$ the voltages arising from contact resistances $R_a\,(\Omega) = 0.5 - 4\Delta I_b\,(\mathrm{A})$ and $R_b = 2.8\ \Omega$ were subtracted from the measured voltages. Here $\Delta I_b = I_b - 20$ mA. For conversion to emission frequencies, junction numbers $N_a = 460$ for stack a and $N_b = 465$ for stack b were used. Every data point is represented by a rectangle of reduced aspect ratio to accommodate the higher density of points along $I_b$ and $V_{r,b}$.

$P_{a,\alpha}(I_a)$ and $P_{b,\alpha}(I_b)$ are the emission powers of the individual stacks if they were independent of each other. The index $\alpha$ indicates whether the signal is detected in channel X or channel Y, i.e., $\alpha$ is either X or Y. $P_{ab,\alpha}(I_a, I_b)$ stands for the additional emission when the stacks are interacting. $P_{a,\alpha}(I_a) + P_{b,\alpha}(I_b)$ constitutes the tartan pattern. The feature of interest is the diagonal line indicating interaction represented by $P_{ab,\alpha}(I_a, I_b)$, which basically represents the interference between the two oscillators.

To convert the current scales to the more-interesting voltage and frequency scales we need to have a good estimate of the number of IJJs in the stack, and we need to properly subtract the voltages arising from contact resistances from the measured voltages $V_a$ and $V_b$. First, we assume that the power oscillations are generically a function of the dominant emission frequencies $f_a$ and $f_b$. Then, in a plot of the bolometric power versus $f_a$ and $f_b$, the tartan pattern would consist of strictly vertical and horizontal features if the junctions were thermally decoupled. Such a coupling occurs, but from previous observations obtained by the monitoring of IVCs of individual stacks and the corresponding emission power over a wide range of bath temperatures [66] we have indications that the dependence of the emission power on the bath temperature is relatively small. We thus ignore the crosstalk between the stacks here. Next, using the Josephson relation, we need to convert this into the voltage drop across the synchronized "active" junctions in a given stack, $V_{r,a}$ and $V_{r,b}$. Assuming that the numbers of these junctions are (at least nearly) constant within our relatively narrow observation window, we are left with the problem to determine $V_{r,a}$ and $V_{r,b}$ from the measured voltages $V_a$ and $V_b$. Both true contact resistances and the voltage across unsynchronized junctions need to be subtracted. These contributions will be nonlinear with respect to the bias currents and may, because of heating, also depend on the biasing condition of the other stack. Given the narrow observation window, we linearize these contributions to "contact resistances" $R_a$ and $R_b$ within the observation window and correspondingly subtract this linear resistance from the measured voltages to obtain, $V_{r,a}$ and $V_{r,b}$. Details are given in Appendix A. For the contact resistances near the voltages of interest, we find $R_a\,(\Omega) = 0.5 - 4\Delta I_b\,(\mathrm{A})$ for stack a (where $R_a$ is in ohms and the current change $\Delta I_b$ is in amperes) and $R_b = 2.8\ \Omega$ for the total contact resistance of stack b. The term $4\Delta I_b$, with $\Delta I_b = I_b - 20$ mA, is induced by the Joule power dissipated in stack b. Figure 5(b) shows the resulting data for the rescaled voltages $V_{r,a} = V_a - R_a I_a$ and $V_{r,b} = V_b - R_b I_b$. To find the junction numbers in stacks a and b, we use the 752.033-GHz water absorption line, which becomes visible when the interferometer setup is flooded with ambient air. The procedure is outlined in detail in Appendix A. For the junction numbers, we obtain $N_a = 460 \pm 1$ for stack a and $N_b = 465 \pm 1$ for stack b.

For lock-in channel X the result of the conversion is shown in Fig. 5(b). In the ($V_{r,a}$, $V_{r,b}$) or, respectively, the ($f_a$, $f_b$) plane, the tartanlike pattern forms vertical and horizontal stripes and the "diagonal" line appears when $f_a$ and $f_b$ (nearly) coincide.

In the next step we remove the tartanlike oscillations from the data in the ($f_a$, $f_b$) plane. We start from the expression

$$P_{\mathrm{tot},\alpha}(V_{r,a}, V_{r,b}) = P_{a,\alpha}(V_{r,a}) + P_{b,\alpha}(V_{r,b}) + P_{ab,\alpha}(V_{r,a}, V_{r,b}). \tag{2}$$

We then extrapolate by an averaging procedure, which is outlined in Appendix B, the tartan pattern over the diagonal line to find the "background" $B_\alpha(V_{\mathrm{r,a}}, V_{\mathrm{r,b}})$, which is given by the emission power of two independent stacks:

$$B_\alpha(V_{\mathrm{r,a}}, V_{\mathrm{r,b}}) = P_{\mathrm{a},\alpha}(V_{\mathrm{r,a}}) + P_{\mathrm{b},\alpha}(V_{\mathrm{r,b}}). \tag{3}$$

For clarity, Fig. 6(a) repeats the measured data in the ($f_\mathrm{a}$, $f_\mathrm{b}$) plane and Fig. 6(b) shows the reconstructed tartan-like pattern for lock-in channel X. We then consider the ratio $S_\alpha(f_\mathrm{a},f_\mathrm{b}) = P_{\mathrm{tot},\alpha}(f_\mathrm{a},f_\mathrm{b})/B_\alpha(f_\mathrm{a},f_\mathrm{b}) - 1$, which yields the power enhancement ($S_\alpha > 0$) or attenuation ($S_\alpha < 0$) in the case of uncoupled IJJ stacks. Figures 6(c) and 6(d) show $S_\alpha(f_\mathrm{a},f_\mathrm{b})$ for, respectively, channel X and channel Y of the lock-in amplifier. The "diagonal" line is the prominent feature in these plots, and we find that $S_\alpha(f_\mathrm{a},f_\mathrm{b})$ can be both positive and negative, with maximum values of about 0.05 in each direction. Further, one notes in Fig. 6(c) vertical lines near $f_\mathrm{b} = 735$, 741, and 748 GHz that have not been captured by the background reconstruction. In Fig. 6(d) similar lines appear near 741 and 748 GHz. These lines correspond to small but sudden changes in $P_{\mathrm{b},\alpha}(f_\mathrm{b})$, which may have been caused by a small number of IJJs in stack b switching from the zero-voltage state to the resistive state, perhaps even by a single junction. In different sweeps of the current through stack b, the jump occurs at slightly different currents and voltages, preventing the background-subtraction procedure from working in the close vicinity of these switching points. Finally, Figs. 6(e) and 6(f), respectively, show $S_\mathrm{X}$ and $S_\mathrm{Y}$ as a function of $f_\mathrm{a}$ and the frequency difference $f_\mathrm{b} - f_\mathrm{a}$. In these plots the power enhancement/attenuation forms a nearly vertical line, with a small residual tilt that has not been captured by our correction procedure to obtain $V_{\mathrm{r,a}}$ and $V_{\mathrm{r,b}}$ and from there $f_\mathrm{a}$ and $f_\mathrm{b}$.

Having found the frequency axes, we can also assign the most-likely cavity resonances that have been excited in the stacks. Generally, for a rectangular geometry the cavity resonance frequencies are given by $f_{\mathrm{cav}} = c_1\sqrt{(p/2W)^2 + (q/2L)^2}$, where $c_1 \approx (6.5\text{–}7) \times 10^7$ m/s is the in-phase mode velocity and the integers $p$ and $q$ represent the number of half-waves of the $c$-axis electric field along, respectively, the width and the length of the stack. The emission occurs near 750 GHz, which requires $p = 1$. For $q$, the most-likely number is 3. One may also consider an inhomogeneous out-of-plane-mode structure consisting of $r$ half-waves in the $z$ direction. For the junction numbers of our experiments, the mode velocity $c_\mathrm{r}$ is about $c_1/r$, requiring $p = 2$ and $q \approx 6$ for $r = 2$ to match the observed emission frequency, and even higher mode indices $p$ and $q$ for $r = 3$. In addition, simulations using coupled sine-Gordon equations persistently yield $r = 1$ and $q = 3$ for the parameters of our stacks; see Appendix C. We thus consider the in-phase mode $r = 1$ as the most-likely scenario.

For the further analysis of $S_\alpha(f_\mathrm{a},f_\mathrm{b})$, as shown in Figs. 6(e) and 6(f), let us first look at the presumed phase synchronization of two IJJ stacks. In an extremely simplified approach we start with an effective Kuramoto model [93,94] of two coupled pointlike identical oscillators. In the model, oscillator a oscillates and radiates at a dressed (i.e., including interactions) angular frequency $\dot{\delta_\mathrm{a}} = \omega_\mathrm{a} + (K/2)\sin\delta$, and oscillator b oscillates at $\dot{\delta_\mathrm{b}} = \omega_\mathrm{b} - (K/2)\sin\delta$. Here, $\delta = \delta_\mathrm{b} - \delta_\mathrm{a}$ is the phase difference between the two oscillators and $K$ is the strength of the mutual interaction. $\omega_\mathrm{a} = 2\pi \times f_\mathrm{a}$ and $\omega_\mathrm{b} = 2\pi \times f_\mathrm{b}$ are the bare frequencies without interaction. In the case of phase-locking, the dressed frequencies are equal, $\dot{\delta_\mathrm{a}} = \dot{\delta_\mathrm{b}}$ (common frequency $f_0$) and we obtain

$$\delta = \sin^{-1}\left(\frac{f_\mathrm{b} - f_\mathrm{a}}{K/2\pi}\right). \tag{4}$$

This constrains the phase difference to the interval $[-\pi/2, \pi/2]$ and implies $|f_\mathrm{b} - f_\mathrm{a}| \leq K/2\pi$ during phase-locking. With respect to emission properties, if we ignore optical path differences, these two oscillators would emit a power $P$ proportional to $|E_\mathrm{a} + E_\mathrm{b}e^{-i\delta}|^2 = E_{0,\mathrm{a}}^2 + E_{0,\mathrm{b}}^2 + 2E_{0,\mathrm{a}}E_{0,\mathrm{b}}\cos(\delta)$, where $E_\mathrm{a} = E_{0,\mathrm{a}}e^{i\delta_\mathrm{a}}$ and $E_\mathrm{b} = E_{0,\mathrm{b}}e^{i\delta_\mathrm{b}}$ denote the complex light fields. The expression may be reformulated as

$$P = P_\mathrm{a} + P_\mathrm{b} + 2\sqrt{P_\mathrm{a}P_\mathrm{b}}\cos(\delta), \tag{5}$$

where $P_\mathrm{a}$ and $P_\mathrm{b}$ denote the power emitted by, respectively, oscillator a and oscillator b. One notices that when $\delta$ approaches $\pm\pi/2$, there is no difference from decoupled oscillators. For the signal enhancement $S$, one expects on this level

$$S = \frac{2\sqrt{P_\mathrm{a}P_\mathrm{b}}}{P_\mathrm{a} + P_\mathrm{b}}\cos(\delta). \tag{6}$$

Inserting Eq. (4) into Eq. (6), one finds that a plot of $S$ versus $f_\mathrm{b} - f_\mathrm{a}$ is just a semicircle ending at $(f_\mathrm{b} - f_\mathrm{a})2\pi/K = \pm 1$. When thermal fluctuations are included, phase-locking will not be achieved over very long times. Particularly, we expect that the phase-locking goes to zero when the dressed frequencies are far from the degeneracy point $f_\mathrm{a} = f_\mathrm{b}$ of the undressed frequencies. In Eq. (6) $\cos(\delta)$ should be replaced by the time average $\langle\cos(\delta)\rangle$, which we can formally also write as $\langle\cos(\delta)\rangle = C(\Delta f)\cos(\delta_\mathrm{f})$, with $C(\Delta f) = \sqrt{\langle\cos\delta\rangle^2 + \langle\sin\delta\rangle^2}$, $\delta_\mathrm{f} = \tan^{-1}(\langle\sin\delta\rangle/\langle\cos\delta\rangle)$, and $\Delta f = f_\mathrm{b} - f_\mathrm{a}$. Then $S$ is given by

$$S = \frac{2\sqrt{P_\mathrm{a}P_\mathrm{b}}}{P_\mathrm{a} + P_\mathrm{b}}C(\Delta f)\cos(\delta_\mathrm{f}). \tag{7}$$

In a more-realistic setting we have to consider that we have two stacks, each consisting of strongly coupled oscillators (the IJJs). In addition, a cavity resonance has built

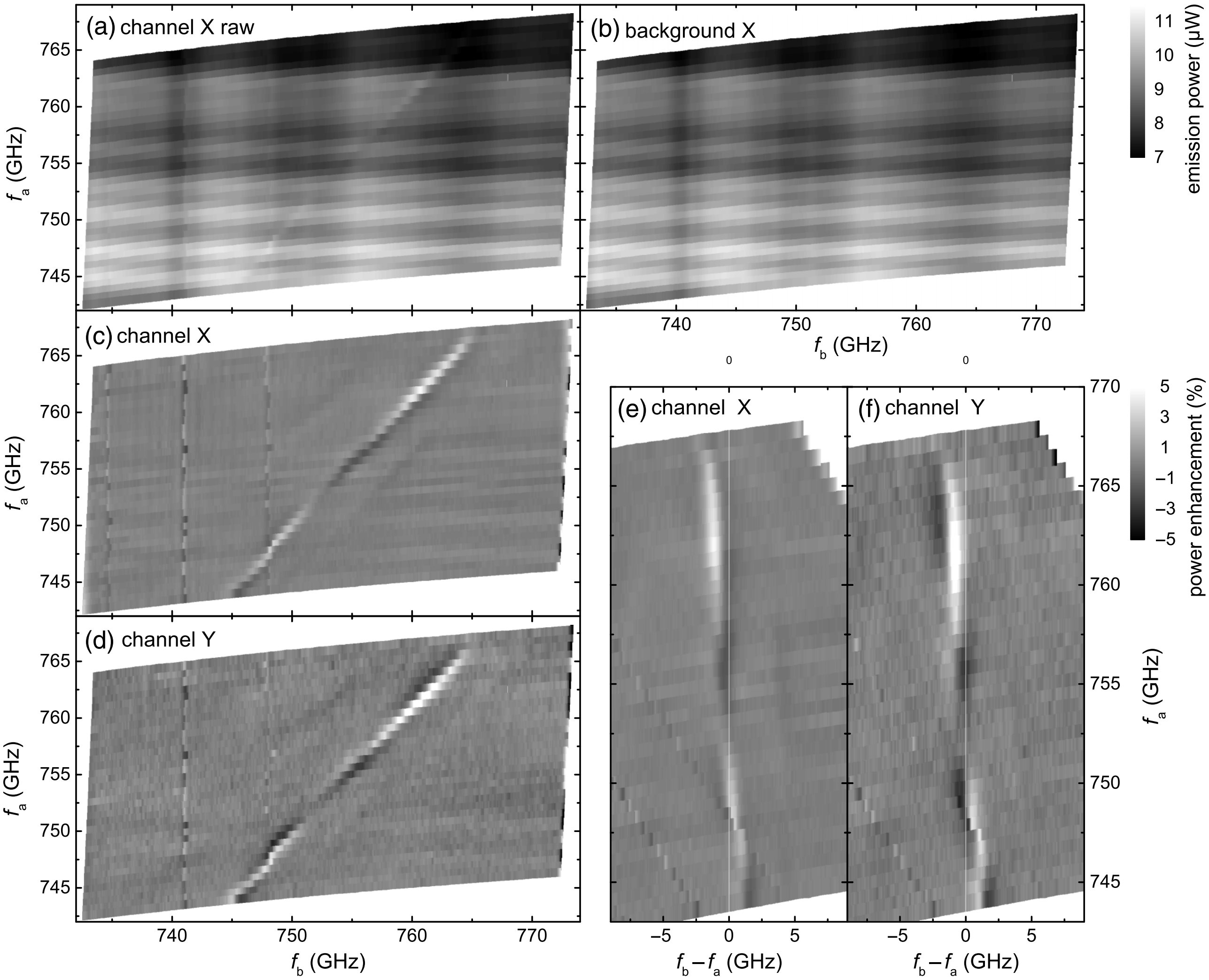

FIG. 6. Emission power (gray scale) versus frequencies $f_a$ and $f_b$. (a) Data as presented in Fig. 5(b). (b) Reconstructed tartan background. (c),(d) Power enhancement $S_\alpha(f_a,f_b)$ of the measured emission relative to the tartanlike background for (a)–(c) is for lock-in channel X and for (d) is for lock-in channel Y. (e),(f) Same data as in(c),(b) but replotted in the $(f_b - f_a, f_a)$ plane. Vertical white lines in (e),(f) indicate $f_b - f_a = 0$.

up in each stack, causing spatial variations of the Josephson phases, and the presence of a hot spot complicates the situation even more. A single stack can be modeled numerically by the use of 3D coupled sine-Gordon equations combined with heat-diffusion equations [66,67]. In the code, the $N$ IJJs in the stack are grouped into $M$ segments, where the $G = N/M$ junctions in a given segment are assumed to oscillate coherently. To approach the situation of two coupled stacks to zero order, we consider two electrically decoupled rectangular stacks separated by one pixel. Details are given in Appendix C. The two stacks share a common continuous segment that can provide mutual coupling. The common segment can be fully superconducting, representing a toy model for a base crystal, or it can be normal-conducting, representing a toy model for the common gold electrode. In both cases we observe mutual synchronization via alternating currents bridging the gap between the stacks, supporting our main observation that mutual synchronization works also in the absence of a common base crystal. Further, the thermal coupling between the stacks through the common segment and the substrate underneath remains intact. The basic result from this model is that the phase $\delta_f$ varies almost linearly between $+\pi$ and $-\pi$ as a function of $f_b - f_a$, and we see a decaying function, which, for simplicity we approximate by a Gaussian for further analysis. Expressed in terms of the frequency difference $f_b - f_a$, the correlation function reads

$$C(\Delta f) = C_0 e^{-[(f_b - f_a)/f_C]^2}, \qquad (8)$$

where $f_C$ is a fit parameter. In the simulations shown in Appendix C, $C_0$ is on the order of 0.5. We further use the linear function $\delta_f = (f_b - f_a)/f_\delta$, where $f_\delta$ is a fit parameter, to describe the functional dependence of $\delta_f$ on $f_b - f_a$.

The final step, before the data shown in Fig. 6 can be analyzed further, is to find an expression analogous to Eq. (7) for the actual lock-in-detected functions $S_X$ and $S_Y$. Details are given in Appendix D. The basic results are the expressions

$$S_X = \frac{P_{X0}}{P_{Xa} + P_{Xb}} C(\Delta f)\cos(\delta_f + \varphi_X) = S_{X0} C(\Delta f)\cos(\delta_f + \varphi_X), \tag{9a}$$

$$S_Y = \frac{P_{Y0}}{P_{Ya} + P_{Yb}} C(\Delta f)\cos(\delta_f + \varphi_Y) = S_{Y0} C(\Delta f)\cos(\delta_f + \varphi_Y), \tag{9b}$$

with $C(\Delta f)$ as in Eqs. (7) and (8). Compared with Eq. (7), there are extra phases $\varphi_X$ and $\varphi_Y$, which are different for channel X and channel Y. They depend on parameters that cannot be extracted from experimentally available data and should be treated as free parameters. Because of the integration over the interfering-beam profiles, the amplitudes $S_{X0}$ and $S_{Y0}$ can go well below 1 and depend on unknown details, so no direct conclusion on the magnitude $C_0$ of the correlation function $C(\Delta f)$ can be made.

Figure 7(a) shows by the solid black (channel X) and dashed gray (channel Y) lines experimental curves of $S_\alpha$ versus $f_b - f_a$ for fixed values of the common frequency $f_0$, where $f_b = f_a$. $S_\alpha$ shows a variation of maximally 5% when the difference frequency $f_b - f_a$ is scanned. For technical reasons (comparatively large current steps between adjacent values of the bias current $I_a$), we used the original curves that were recorded at a fixed bias current $I_a$; i.e., compared with the plots in Figs. 6(e) and 6(f) the line scans are slightly tilted to the horizontal direction, which, however, makes little difference to the data evaluation in the small-frequency-difference regime we show in Fig. 7(a). The currents $I_a$ are indicated. The corresponding common frequencies $f_0$ are indicated in Fig. 7(b). The six curves are vertically offset for clarity. Note that in the spirit of phase-locking, as described above, the horizontal axis should display the difference of the bare frequencies (decoupled oscillators) rather than the measured difference of the dressed frequencies (coupled oscillators). However, this difference is unresolvable in the experiments presented and we thus do not distinguish them here. Further, the experimental data are not centered at $f_b - f_a = 0$. We attribute this to residual errors in our evaluation procedure to extract $f_a$ and $f_b$. Inaccuracies can arise, for example, because the junction numbers $N_a$ and $N_b$ are not constant within our measurement observation window of bias currents and voltages; see Fig. 5(a). Below we provide evidence that these changes are observable but small; see Figs. 6(c) and 6(d). A more-dominant source of inaccuracy is probably the determination of the linearized “contact resistance,” which involves real contact resistances between the stack and the gold electrodes but also junctions not contributing to the observed emission.

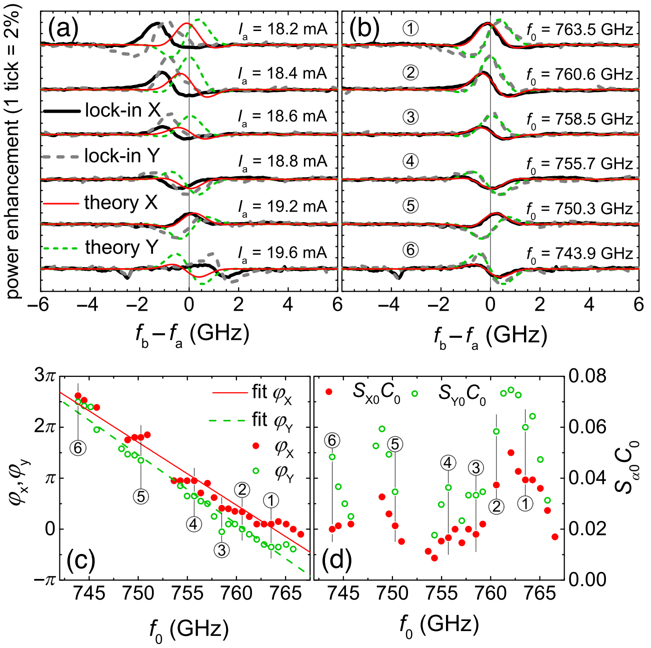

FIG. 7. Evaluation of power enhancement. (a),(b) $S_\alpha$ versus frequency difference $f_b - f_a$ for six values of the common frequency $f_0$, where $f_b = f_a$. Currents $I_a$ through stack a are also indicated. Curves for different values of $f_0$ are vertically offset for clarity. Experimental data for channel X and channel Y are given by the solid black and the dashed gray lines, respectively. Solid red and dashed green lines represent corresponding theoretical curves obtained with Eqs. (9a) and (9b). Model parameters are chosen to best reproduce the shape of the experimental curves. (a) Original data. In (b) the experimental curves are shifted to be on top of the theoretical curves. (c) Phases $\varphi_X$ and $\varphi_Y$ versus $f_0$. Linear fits are shown by the solid lines. (d) Factor $S_{\alpha 0}C_0$ required to match the amplitudes of the experimental and theoretical curves of $S_\alpha$ versus the common frequency $f_0$. Labels 1–6 in (c),(d) indicate line scans 1–6 in (b).

Accepting these errors, to further compare the experimental data with the theoretical expressions in Eqs. (9a) and (9b), we first find parameters that optimally reproduce the shape of $S_\alpha$ versus $f_b - f_a$. We first globally set $f_C = 0.9$ GHz and $f_\delta = 0.58$ GHz for all curves. We then adjust the phases $\varphi_X$ and $\varphi_Y$ for each curve and individually adjust the factor $S_{\alpha 0}C_0$ to match the amplitude of the theoretical curves and the experimental ones. The results are shown by the solid red and dashed green lines representing, respectively, channel X and channel Y. As dictated by Eqs. (9a) and (9b) the theoretical curves are centered at $f_b - f_a = 0$. For a better comparison, Fig. 7(b) shows the same data but with the experimental curves shifted to be on top of the theoretical curves. The agreement is excellent, giving us confidence that the essential physics is captured by Eqs. (9a) and (9b).

Figure 7(c) displays the phases $\varphi_X$ and $\varphi_Y$ versus the common frequency $f_0$. Apart from the constant offset, the basic observation is that both $\varphi_X$ and $\varphi_Y$ are, within our resolution, linear functions with slopes $d\varphi_\alpha/df_0$ of, respectively, $-2\pi/16.2$ GHz and $-2\pi/14.8$ GHz for channel X and channel Y. The linear dependence of $\varphi_X$ and $\varphi_Y$ on $f_0$ is in line with our assumption that between the location of the oscillators and the location of the bolometer, substantial geometric phase differences (of unknown origin) have built up. Interpreted in terms of optical path differences between the two stacks, the observed slopes imply an *average* path difference $\Delta l$ of 2 cm, which is still too large to be explained easily. Finally, the amplitudes $S_{\alpha 0}C_0$ are displayed in Fig. 7(d). The amplitude can exceed 7%, but near 755 GHz can also be below 2%. The overall dependence of $S_{\alpha 0}C_0$ on $f_0$ is not very systematic and may have been caused by small drifts and fluctuations on the timescale of several minutes or so in our detection scheme. While the effect for the overall detected power is small, such fluctuations are strongly enhanced when we calculate $S_{\alpha 0}C_0$. More importantly, the overall small values of $S_{\alpha 0}C_0$ are consistent with our assumption that the wave fronts created by the two stacks show very strong spatial phase gradients, leading to destructive interference in the detection plane.

We finally mention that the numerical simulations outlined in Appendix C delivered identical time-averaged voltages and Josephson frequencies between the two stacks only within part (about less than half) of the frequency interval $f_C$ spanned by the Gaussian. The true locking range $|f_b - f_a|$ may thus be below 200 MHz, which is consistent with our previous measurements with the SIR, where two individual lines appeared when their emission frequencies differed by around 100 MHz.

## IV. SUMMARY AND CONCLUSIONS

As our main result we observed mutual synchronization of two stacks of IJJs in a standalone geometry without a common base crystal. The distance between the stacks is 200 μm, and they share a common gold electrode presumably providing mutual coupling. Some preliminary data were obtained with a high-spectral-resolution setup using a superconducting integrated receiver at around 650 GHz [89]. The measurements presented in this paper are based on a bolometric emission setup and extend the observation of phase-locking for the same sample to frequencies between 745 and 765 GHz. Since the present setup is a standard one available in many laboratories, our measurement protocol and the subsequent detailed analysis may be helpful for many other groups working in the field.

We find that phase correlations between the two stacks have a Gaussian shape and occur on the scale of about ±0.4 GHz relative to the center frequencies where the bare (uncoupled) frequencies of the two oscillators coincide. We give arguments that the wave fronts emitted by the two stacks have very strong spatial gradients, leading to destructive-interference effects. We speculate that the origin lies in the excited cavity modes, which, on the one hand, seem to be necessary for synchronization but, on the other hand, lead to a strongly varying Josephson phase along the edges of each stack.

In the experiments described and analyzed in this paper, the thermal coupling was still limited by the glue used to mount the sample. However, our observation that the mutual synchronization of IJJ stacks separated by relatively large distances can be induced by a common gold electrode rather than a base crystal could relax the notorious problem of Joule heating in an improved layout, because the gold layer can provide a much-better thermal coupling to a substrate than the BSCCO base crystal. For example, the gold layer could be made thicker and brought into direct contact with a thermally-well-anchored (and perhaps even metallic) substrate. The stacks emit radiation through the lens in opposite directions, so such a substrate would not block radiation. In addition, the problem of strong spatial phase gradients may be relaxed if the individual stacks in a multistack array are made considerably smaller in lateral size than the presently used ones. Thus, the gold layer–mediated coupling may open new possibilities to synchronize a large number of IJJs to increase the emission power to values well above 1 mW.

## ACKNOWLEDGMENTS

We gratefully acknowledge financial support by the Deutsche Forschungsgemeinschaft via Projects No. KL930/13-2 and No. KL930/17-1, the Scientific and Technological Research Council of Turkey (Grant No. 2219-2020/2-1059B192000817), the Research Fund of Inonu University under Grant Contract No. FOA-2023-3260, the Russian Science Foundation (Grant No. 19-19-00618), the National Key R&D Program of China (Grant No. 2021YFA0718802), the National Natural Science Foundation of China (Grant No. 62288101), and Jiangsu Key Laboratory of Advanced Techniques for Manipulating Electromagntic Waves. R.W. acknowledges financial support from the Carl Zeiss Stiftung.

## APPENDIX A: CONVERSION FROM CURRENT AXES TO VOLTAGE AND FREQUENCY AXES, DETERMINATION OF CONTACT RESISTANCES, AND JUNCTION NUMBERS

The voltages $V_a$ and $V_b$ we measure contain parasitic contributions from the contact resistances and perhaps from IJJs that do not contribute to the (coherent) radiation of the single stacks. We write these contributions as $V_{p,a} = R_a I_a$ for stack a and as $V_{p,b} = R_b I_b$ for stack b. We thus have $V_{r,a} + R_a I_a = V_a$ and $V_{r,b} + R_b I_b = V_b$. $V_{r,a}$

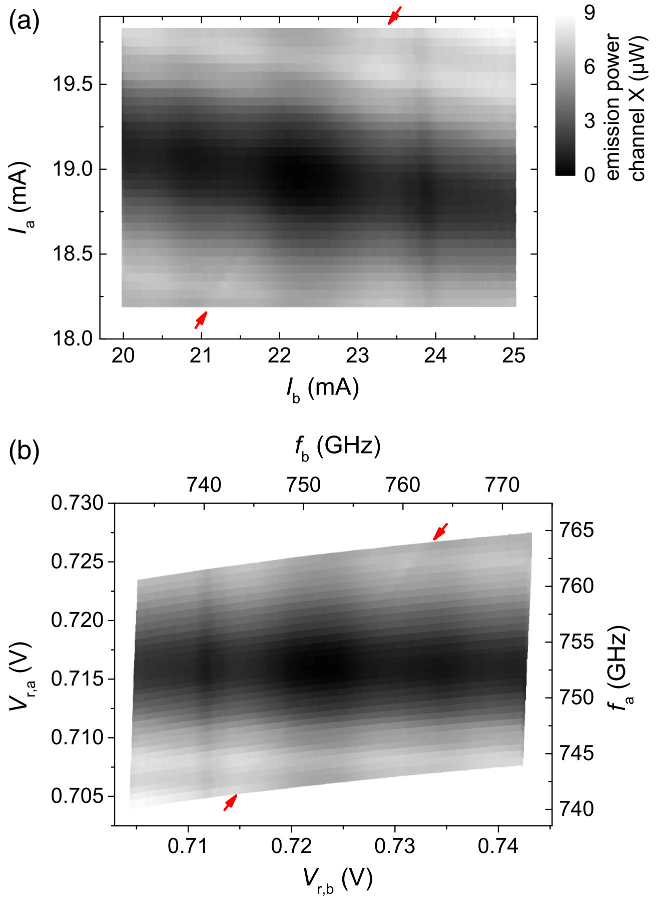

FIG. 8. For lock-in channel X: emission data for the two stacks biased at the same time while the setup was exposed to humid air. (a) Bolometric power as a gray scale plotted against stack currents $I_a$ and $I_b$. (b) Bolometric data as a function of the rescaled voltages $V_{r,a}$ and $V_{r,b}$ (left and bottom axes) and the corresponding emission frequencies $f_a$ and $f_b$ created from the voltage axes with $N_a = 460$ and $N_b = 465$. (right and top axes).

and $V_{r,b}$ are the voltages of interest. In general, $R_a$ and $R_b$ will be nonlinear with respect to the bias currents and may, because of heating, also depend on the biasing condition of the other stack. We linearized these contributions, which is appropriate considering the narrow measurement windows used for the emission experiments. In particular, the current range $\Delta I_a$ is very narrow for stack a and the cross-contribution from stack a to stack b is minor and thus ignored here.

To determine the linearized $R_a$ and $R_b$, we use previous observations that the quasiperiodic oscillations in the detected emission power as a function of either current or voltage—see Figs. 4(b) and 4(c)—are actually functions of the frequencies of the emitted radiation. This means that in a plot of the detected radiation power versus $V_{r,a}$ and $V_{r,b}$ they should occur as horizontal and vertical stripes. Actual values for $R_a$ and $R_b$ that fulfill this condition to good accuracy within the current ranges $17.9 \text{ mA} < I_a < 19.7 \text{ mA}$ and $20 \text{ mA} < I_b < 25 \text{ mA}$ and used to generate Fig. 5(b) are given by $R_a\,(\Omega) = 0.5 - 4\Delta I_b\,(\text{A})$ and $R_b = 2.8\ \Omega$, where $\Delta I_b = I_b - 20$ mA. With current for stack b maximally varying by $\Delta I_b = 5$ mA, $R_a$ varies in the range from 0.48 to 0.5 Ω.

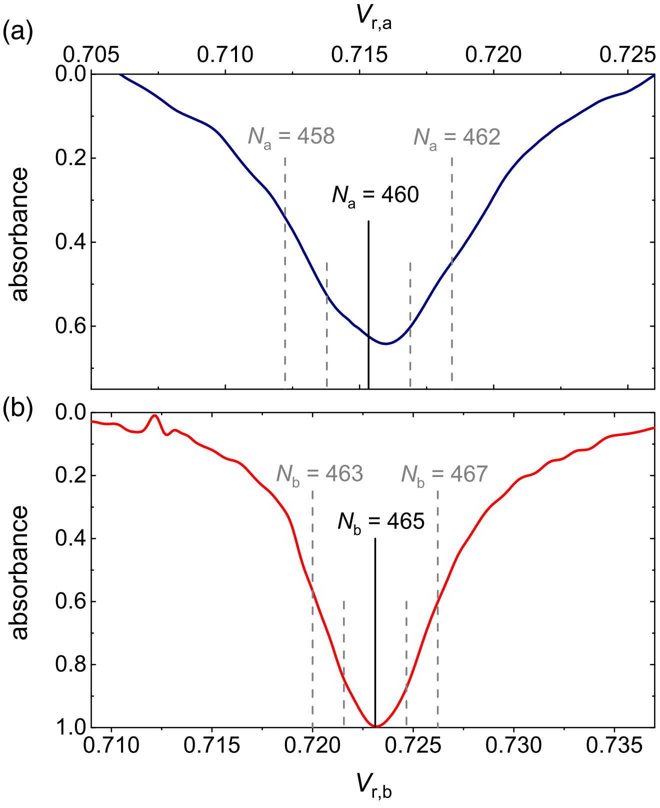

FIG. 9. Absorbance as a function of rescaled stack voltages for (a) stack a and (b) stack b. Voltages corresponding to different junction numbers are indicated by vertical lines, the solid ones indicating the most-likely numbers.

To convert voltages $V_{r,a}$ and $V_{r,b}$ to emission frequencies, the junction numbers $N_a$ and $N_b$ must be known. To find these numbers, in a first step we measure the emission frequencies using our Fourier-transform interferometer and relate them to voltages $V_{r,a}$ and $V_{r,b}$. In a second step we refine the calibration by using the water-vapor absorption line at $f_{\text{water}} \approx 752.033$ GHz, which becomes visible in absorption spectra when the interferometer is flooded with (humid) air rather than with nitrogen gas.

To do so we have both oscillators in the emitting state, as shown in Fig. 5, where the bias currents through the two stacks are varied over some range while the setup is flooded with nitrogen. We then perform the same measurement with the setup exposed to humid air. The result is shown in Fig. 8(a) in the $(I_a, I_b)$ plane. Figure 8(b) shows the same data in the $(V_{r,a}, V_{r,b})$ plane. As outlined in Appendix B, the data in Figs. 5 and 8 allow reconstruction of the terahertz power emitted by the individual stacks as a function of, respectively, $V_{r,a}$ and $V_{r,b}$. Using these curves, we create the normalized difference $(P_{k,\mathrm{N}_2} - P_{k,\mathrm{air}})/(P_{k,\mathrm{N}_2} + P_{k,\mathrm{air}})$, with $k = (\mathrm{a}, \mathrm{b})$. This difference constitutes the absorbance and is plotted in Fig. 9 for the two stacks versus, respectively, voltages $V_{\mathrm{r,a}}$ and $V_{\mathrm{r,b}}$. Figure 9(a) is for stack a and Fig. 9(b) is for stack b. The absorption line for stack a leads to $N_{\mathrm{a}} = 460 \pm 1$. For stack b, $N_{\mathrm{b}} = 465$ marks the most-likely junction number. Using these values, we create the frequency axes shown in Figs. 5(b), 6, and 8(b).

## APPENDIX B: RECONSTRUCTION OF THE EMISSION BACKGROUND CREATED BY UNLOCKED STACKS

To find the tartanlike background of the recorded emission power in the $(V_{\mathrm{r,a}}, V_{\mathrm{r,b}})$ plane, we start from Eq. (2):

$$P_{\mathrm{tot},\alpha}(V_{\mathrm{r,a}}, V_{\mathrm{r,b}}) = P_{\mathrm{a},\alpha}(V_{\mathrm{r,a}}) + P_{\mathrm{b},\alpha}(V_{\mathrm{r,b}}) + P_{\mathrm{ab},\alpha}(V_{\mathrm{r,a}}, V_{\mathrm{r,b}}), \tag{2}$$

where $B_\alpha(V_{\mathrm{r,a}}, V_{\mathrm{r,b}}) = P_{\mathrm{a},\alpha}(V_{\mathrm{r,a}}) + P_{\mathrm{b},\alpha}(V_{\mathrm{r,b}})$ forms the background signal created by two independent IJJ stacks and $\alpha$ stands for either channel X or channel Y. As we know from emission measurements of the stacks being biased one at a time, $P_{\mathrm{a},\alpha}(V_{\mathrm{r,a}})$ and $P_{\mathrm{b},\alpha}(V_{\mathrm{r,b}})$ exhibit modulations as a function of, respectively, $V_{\mathrm{r,a}}$ and $V_{\mathrm{r,b}}$. Further, these oscillations appear on top of a constant background that, when both stacks are biased simultaneously, cannot be unambiguously attributed to either stack a or stack b. For simplicity, we add this contribution to stack a in the fit procedure.

We thus, independently for channel X and channel Y, parameterize $P_{\mathrm{a},\alpha}(V_{\mathrm{r,a}})$ as the sum of several Gaussian curves plus a linear term:

$$P_{\mathrm{a},\alpha}(V_{\mathrm{r,a}}) = b + mV_{\mathrm{r,a}} + \sum_{n=1}^{N_A} a_{n,\mathrm{a}} \exp\left[-\left[\frac{V_{\mathrm{r,a}} - v_{n,\mathrm{a}}}{c_{n,\mathrm{a}}}\right]^2\right], \tag{B1}$$

with the number of summands $N_A = 22$.

For $P_{\mathrm{b},\alpha}(V_{\mathrm{r,b}})$ we use

$$P_{\mathrm{b},\alpha}(V_{\mathrm{r,b}}) = \sum_{n=1}^{N_B} a_{n,\mathrm{b}} \exp\left[-\left[\frac{V_{\mathrm{r,b}} - v_{n,\mathrm{b}}}{c_{n,\mathrm{b}}}\right]^2\right], \tag{B2}$$

with the number of summands $N_B = 24$.

The resulting functions $P_{\mathrm{a,X}}(V_{\mathrm{r,a}})$ and $P_{\mathrm{b,X}}(V_{\mathrm{r,b}})$ with the best fitting parameters are plotted in Figs. 10(a) and 10(b), respectively. The background $B_{\mathrm{X}}(V_{\mathrm{r,a}}, V_{\mathrm{r,b}})$ evaluated at the voltages of all data points is plotted in Fig. 6(b) with voltages converted to frequencies. Figures 10(c) and 10(d) show the corresponding functions $P_{\mathrm{a,Y}}(V_{\mathrm{r,a}})$ and $P_{\mathrm{b,Y}}(V_{\mathrm{r,b}})$ for channel Y.

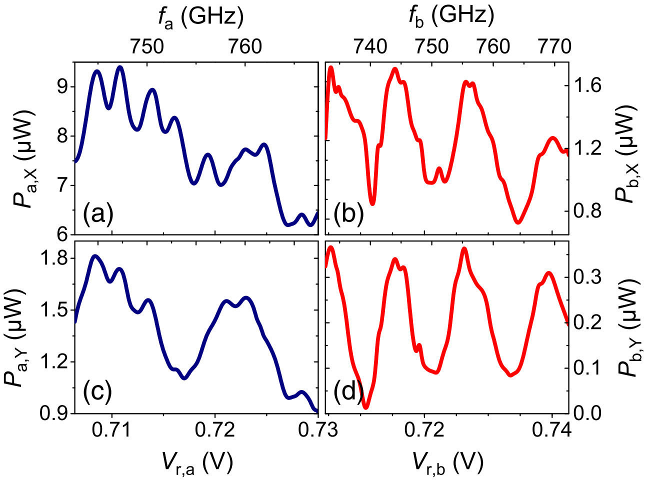

FIG. 10. (a) $P_{\mathrm{a,X}}$, (b) $P_{\mathrm{b,X}}$, (c) $P_{\mathrm{a,Y}}$, and (d) $P_{\mathrm{b,Y}}$, as obtained from the fitting procedure.

As mentioned, we cannot assign the constant $b$ unambiguously to stacks a and b. A redistribution can be made from the analysis of the humid-air absorption data discussed in Appendix A. By simply requiring that the absorption should not be negative, we find that for channel X a constant offset of 0.625 μW should be subtracted from stack a and added to stack b. For channel Y the corresponding number is 0.025 μW. The necessary corrections strongly depend on actual fit results.

For completeness, Fig. 11(a) shows the original emission data for channel Y in the $(V_{\mathrm{r,a}}, V_{\mathrm{r,b}})$ plane, while Fig. 11(b) shows the reconstructed background $B_{\mathrm{Y}}(V_{\mathrm{r,a}}, V_{\mathrm{r,b}})$.

We finally note that we have also 2D adjacent averaging methods to reconstruct the background. The results for the constituting functions and the reconstructed background are very similar. We are thus confident that the reconstruction is robust and does not suffer from major artifacts.

## APPENDIX C: MINIMAL MODEL FOR MUTUAL PHASE-LOCKING AND SIMULATION RESULTS

In the following we substantiate the expression

$$S = \frac{2\sqrt{P_{\mathrm{a}}P_{\mathrm{b}}}}{P_{\mathrm{a}} + P_{\mathrm{b}}} C(\Delta f) \cos(\delta_{\mathrm{f}}) \tag{7}$$

used in the main part of the paper, with a focus on the Gaussian approximation for $C(\Delta f)$, plus the linear approximation $\delta_{\mathrm{f}} = (f_{\mathrm{b}} - f_{\mathrm{a}})/f_\delta$.

To simulate two coupled stacks we start from 3D coupled sine-Gordon equations combined with heat-diffusion equations [66,67]. In the code we use, the $N$ IJJs in the stack are grouped into $M$ segments, where the $G = N/M$ junctions in a given segment are assumed to oscillate coherently. The IJJs are stacked in the $z$ direction and

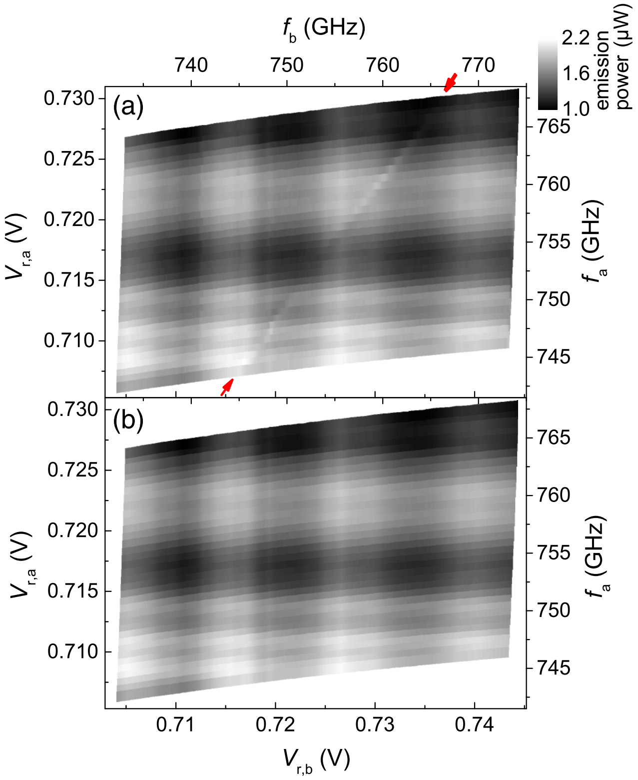

FIG. 11. (a) Raw emission data for channel Y. (b) Reconstructed tartanlike background for channel Y.

extend over distances $L$ and $W$ in the $(x, y)$ direction. For a single stack, the electromagnetic part of the equation reads

$$Gsd\vec{\nabla}\left(\frac{\vec{\nabla}\dot{\gamma}_n}{\rho_{ab}(T)}\right) + G\lambda_k^2\vec{\nabla}\left[n_s(T)\cdot\vec{\nabla}\gamma_n\right] = \left(2 + \frac{G^2\lambda_k^2 n_s(T)}{\lambda_c^2}\right)j_{z,n} - j_{z,n+1} - j_{z,n-1}, \tag{C1a}$$

with

$$j_{z,n} = \frac{\beta_c}{G}\ddot{\gamma}_n + \frac{\dot{\gamma}_n}{\rho_c(T)} + j_{z,n}^N + j_{c,n}(T)\sin(\gamma_n). \tag{C1b}$$

The nabla operators stand for partial derivatives with respect to the $x$ and $y$ coordinates and $n$ is the number of segments. $\gamma_n$ is the Josephson phase difference across a single junction in segment $n$. $s = 1.5$ nm and $d = 0.3$ nm are, respectively the interlayer distance and the thickness of a superconducting layer, $\lambda_k \approx 1.7$ μm is the kinetic length, and $\lambda_c \approx 300$ μm is the $c$-axis penetration depth. $n_s$ is the Cooper-pair density, normalized to its 4.2-K value. $\rho_{ab}$ and $\rho_c$ denote the normalized in-plane and $c$-axis resistivities, and $\beta_c$ is the McCumber parameter. The first term on the left-hand side of Eq. (C1a) represents the (inductive) coupling via in-plane quasiparticle currents, while the second term is due to the coupling via supercurrents.

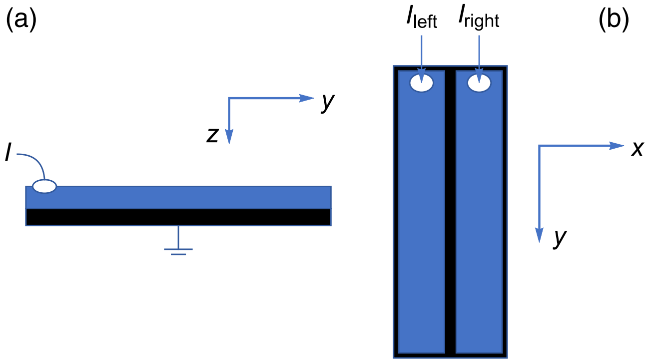

FIG. 12. Geometry of two stacks located on a common segment: (a) side view; (b) top view. In (a) the black rectangle represents the uncut base segment.

Equations (C1a) and (C1b) form the coupled sine Gordon equations, with the $c$-axis currents given by Eq. (C1b). Here, the terms on the right-hand side represent the densities of displacement currents, quasiparticle currents, a noise current, and the Josephson current. Various parameters depend on the local temperature $T$ as indicated. The Joule heat power density $q$ produced by the resistive in-plane and out-of-plane currents, plus the Joule heat generated by currents through a bond wire attached to the uppermost layer of the stack enters the heat-diffusion part of the equations:

$$c\dot{T} = \vec{\nabla}\left[\kappa(T)\vec{\nabla}T\right] + q(T), \tag{C2}$$

where $\kappa$ is the (anisotropic) heat conductivity. Equations (C1a), (C1b) and (C2) are solved simultaneously.

To obtain a certain value of, say, the dc voltage across the stack, we first perform an initialization sequence in the absence of Josephson currents in order to get an initial guess of the temperature distribution in the stack. We then propagate Eqs. (C1a), (C1b) and (C2) in time over about 20 000 periods of the Josephson oscillations to relax the system and then take time traces over another 20 000 periods to obtain time averages and other quantities. More details are given in Refs. [66,67].

To describe two coupled stacks we start from a solid stack of length $L$ and width $2W$ and consider $M + 1$ segments. The geometry is sketched in Fig. 12. We remove the coupling mediated by the terms on the left-hand side of Eq. (C1a) in the upper $M$ segments along a cut extending in the $y$ direction; i.e., we do not allow supercurrents and resistive currents to flow from the right side of the left stack to the left side of the right stack. We leave the lowest segment intact. This constitutes two decoupled $M$-segment stacks located on a common base segment, the lower surface of which we assume to be grounded.

When we keep the electrical parameters as given in Eqs. (C1a) and (C1b), we have a minimal model for two side-by-side stacks located on a common base crystal. Further, to mimic a normal-conducting segment, we interrupt the supercurrent flow between the two stacks by setting also for the base segment the second term on the left-hand side of Eq. (C1a) to zero and null the Josephson current by setting the current density $j_c(T)$ to zero. For a gold layer one should ideally replace $\rho_{ab}$ and $\rho_c$ by the gold resistivities. However, it turned out that particularly a change in $\rho_c$ by orders of magnitude results in unacceptable computing times. We thus just reduced $\rho_{ab}$ and $\rho_c$ by a factor of 100 in the simulations shown in Figs. 13–16.

Note that in our toy model the two stacks remain coupled thermally. Their effective distance is set by the discreteness of our computation scheme, which amounts to 50 μm for the parameters used. This is on the order of but not larger than the spatial extension of thermal gradients seen for our thermal parameters [66,67].

In the simulations shown in Figs. 13–16 we describe each stack only by a single pixel in the $x$ direction. In other words, we model two coupled 2D stacks. For the discretization in the $y$ direction, we use 50 points. The (independent) $M = 20$ segments contain $N = 700$ IJJs, i.e., $G = 35$. This constitutes a base segment with a thickness of 35 layers, i.e., 50 nm. The bath temperature for the calculations is 50 K, and we use $L = 300$ μm and $W = 50$ μm. These parameters do not exactly match the experiment. Particularly, a bath temperature of 50 K was chosen to obtain stable low-bias and high-bias regimes involving cavity resonances just by our changing the bias current.

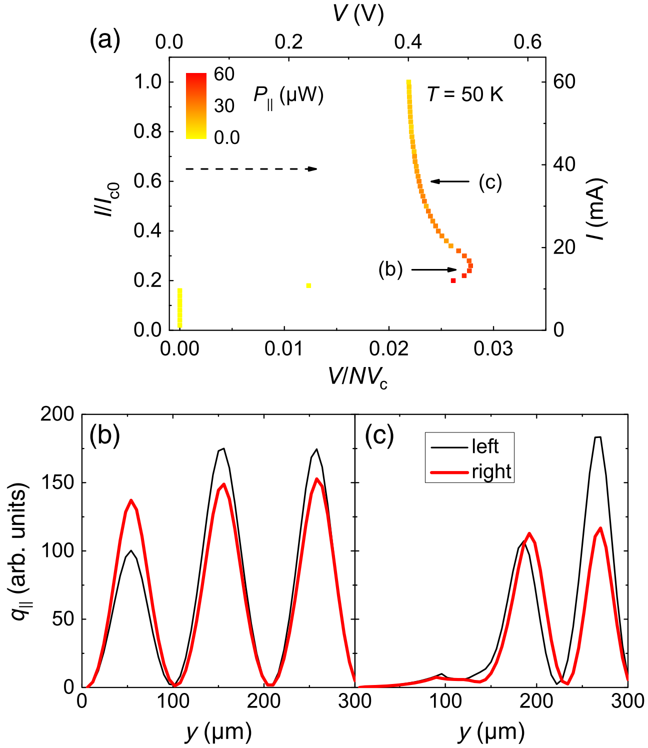

FIG. 13. (a) Simulated current-voltage characteristic of the uncut 300 × 100 $\mu m^2$ stack at a bath temperature of 50 K. The color scale indicates the power dissipated by in-plane currents. The horizontal dashed arrow indicates switching from the zero-voltage state to the resistive state at the 50-K critical current. The horizontal solid arrows indicate the bias points used for biasing the left stack after cutting. (b),(c) Simulation results for the two 300 × 50 $\mu m^2$ stacks coupled via a normal-conducting base segment. (b) Dissipated power density of the resistive in-plane currents for bias $i_{\text{left}} = 0.24$ and $i_{\text{right}} = 0.235$. (c) Dissipated power density of the resistive in-plane currents for bias $i_{\text{left}} = 0.6$ and $i_{\text{right}} = 0.58$.

Figure 13 shows some results to characterize the stacks investigated. Figure 13(a) displays the 50-K IVC of the $L \times 2W$ stack before cutting. On the left vertical axis the current is given in units of the 4.2-K value $I_{c0} = 60$ mA of the critical current, while the right axis displays the bias current in dimensioned units. The voltages displayed on the lower axis are normalized to the characteristic voltage $V_c = I_{c0}R$, where $R = 0.5$ Ω is the 4.2-K value of the $c$-axis resistance per junction. The top axis gives the total voltage of the stack containing 700 IJJ in dimensioned units. The color scale indicates the time-averaged power of the resistive in-plane currents dissipated in the stack. One notes that there is a significant power over a wide range of bias currents, which was one of the reasons for fixing the parameters of the model to the present values. The displayed IVC is obtained by our sweeping the bias current from large values down to zero, i.e., it represents the outermost return branch of the (multivalued) IVC. The horizontal dashed line indicates the 50-K critical current that would have appeared for a bias current increasing from zero. The horizontal solid lines indicate special values of the normalized bias current of 0.24 and 0.6. The lower value is located in the low-bias regime, while the higher one is in the regime where a hot spot covers about half of the stack. We use these values as a starting point for our simulations, where we fix the current to the values in the "left" stack while varying the current through the "right" stack.

Figure 13(b) shows the simulated power density dissipated by in-plane currents versus the $y$ coordinate for normalized bias currents $i_{\text{left}} = 0.24$ and $i_{\text{right}} = 0.235$. The stacks are coupled via the normal-conducting base layer. One observes pronounced oscillations that indicate that a standing wave of the electric field with three half-waves along the $y$ direction has been excited in both stacks. This wave profile was persistent in the whole range of bias currents we investigated in the low-bias regime. In the special case we show here, the integrated power was about 92 μW in the left stack and about 88 μW in the right stack. Figure 13(c) shows analogous data for the high-bias regime, with $i_{\text{left}} = 0.6$ and $i_{\text{right}} = 0.58$. The integrated power was about 52 μW in the left stack and about 41 μW in the right stack. There is a small cusp in the power densities near $y = 100$ μm, left of which the temperature in the stacks has exceeded the critical temperature of 85 K. Also in the high-bias regime the observed oscillations are persistent over the range of bias currents studied.

Figure 14 displays the dc voltages across the individual segments versus the segment number for four different scenarios. To obtain these voltages we average, for a given segment, the time derivative of the Josephson phase over time and the "cold" parts of the segment, where the local temperature is below the critical temperature. This restriction is necessary, because in the normal-conducting part there are nonzero in-plane dc voltages that would spoil spatial averaging. In Fig. 14(a) we consider the low-bias regime, where the two stacks are coupled and biased at slightly different (normalized) currents $i$ of 0.24 and 0.235. For the left stack, biased at $i = 0.24$, the normalized dc voltage, displayed on the left axis, is the same for segments 9–20, while the dc voltage of segments 1–8 has a higher value. This shows that only a part of the segments in the stack is locked. The right axis shows the corresponding Josephson frequencies, which are near 400 GHz for the locked segments. The dc voltages across the segments of the right stack, biased at $i = 0.235$, behave similarly, and in addition, the voltages across both stacks coincide for segments 9–20. In our simulations we have the possibility to remove also the mutual coupling mediated by the base segment. The result is shown in Fig. 14(b). Apart from decoupling, all other conditions for the simulations remained the same, including the sequence of random numbers introduced by the noise current. The overall behavior is the same as for the coupled case, but now segments 8–20 (left stack) and 7–20 (right stack) are locked within the individual stacks. However, the dc voltages and Josephson frequencies of the two stacks never coincide, as should be expected for the different currents used to bias stack a and stack b, respectively. Figures 14(c) and 14(d) show analogous graphs for the high-bias regime.

To investigate the mutual phase-locking more systematically, we next fix the bias current through the left stack while sweeping the current through the right stack. Figure 15 shows the corresponding data. Somewhat arbitrarily we monitor the dc voltages across segment 11 for, respectively, the left stack and the right stack. As seen, for example, in Fig. 14, this segment is inside the locked part of the individual stacks. In Fig. 15 we have converted these voltages to frequency, using the Josephson relation. Figure 15(a) is for the low-bias regime, while Fig. 15(b) is for the high-bias regime. In Fig. 15(a) the normalized bias current through the left stack is kept at 0.24, and the current through the right stack is varied between 0.23 and 0.25. The solid black squares and solid red circles are for, respectively, the left stack and the right stack and were obtained for a mutual coupling mediated by the normal-conducting base segment. We see identical voltages (frequencies) for both stacks between $i_{\text{right}} = 0.235$ and $i_{\text{right}} = 0.245$, indicating phase-locking. Outside this regime the voltages and Josephson frequencies differ. The open green squares and open circles are for the decoupled case and yield, in the language of the Kuramoto model, the "bare frequencies" of the two oscillators. We see that these frequencies can differ substantially from the "dressed frequencies" in the coupled case. Figure 15(b) shows the corresponding data for the high-bias regime where the left stack was biased at a normalized current of 0.6, while the current through the right stack was varied between 0.55 and 0.65. The overall behavior is similar to that in the low-bias case. One also notes that in both Fig. 15(a) and Fig. 15(b) the data look noisy. It turned out that when we repeated calculations as shown in Fig. 15 or Fig. 16 for a *different* sequence of random numbers entering via the $c$-axis noise current for otherwise the same initial conditions, we ended up with slightly different voltages. While this is unproblematic in terms of absolute voltages and/or frequencies, it is problematic for the high-resolution analysis of mutual phase-locking. The reason is that, depending on the history, slightly different profiles of the local stack temperatures and the Josephson phases were established and seem to be long-lived on the scale of our integration times (which, however, in dimensioned units are only on the order of 50 ns and are thus 7 orders of magnitude shorter than in our experiments).

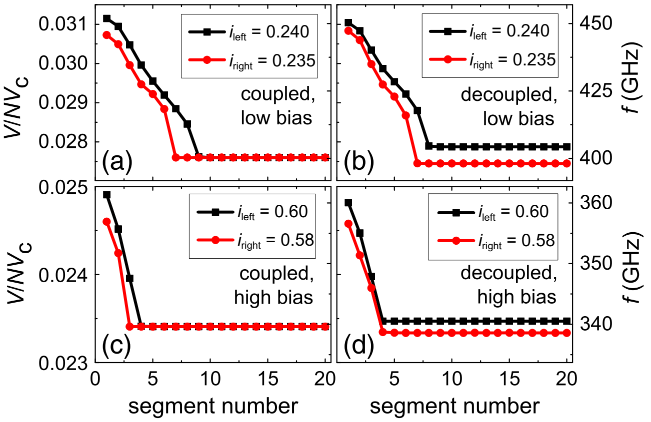

FIG. 14. dc voltage (left axes) and corresponding Josephson frequency (right axes) across individual segments versus the segment number (bottom axes) for (a),(b) the low-bias regime and (c),(d) the high-bias regime. In (a),(c) the stacks are coupled via a normal-conducting base segment, and in (b),(d) the stacks are completely decoupled electrically.

To address the problem, we performed each calculation five times, using different sequences of random numbers. The result for the analysis of phase-locking is shown in Fig. 16. Here we first defined the quantities $\cos\delta$ and $\sin\delta$, where $\delta$ is the difference of the momentary and local Josephson phases in adjacent points in the left stack and the

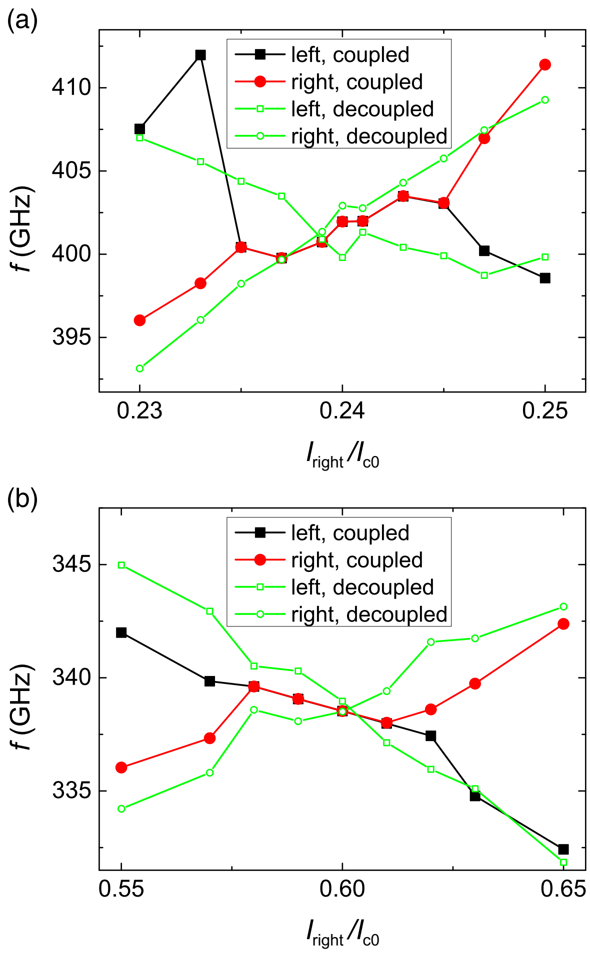

FIG. 15. dc voltages across segment 11 in the left stack and the right stack, converted to the Josephson frequencies, for a fixed bias current (a) $i_{\mathrm{left}} = 0.24$ and (b) $i_{\mathrm{left}} = 0.6$ through the left stack and a variable bias current through the right stack.

right stack. We then averaged these quantities over the cold parts of the stack and over time to obtain the average quantities $\langle\cos\delta\rangle$ and $\langle\sin\delta\rangle$, which we used to define the correlation function $C(\Delta f) = \sqrt{\langle\cos\delta\rangle^2 + \langle\sin\delta\rangle^2}$ and the phase $\delta_{\mathrm{f}} = \tan^{-1}(\langle\sin\delta\rangle/\langle\cos\delta\rangle)$. These quantities were introduced in the main text. Here $\Delta f = f_{\mathrm{b}} - f_{\mathrm{a}}$ is the difference of the bare Josephson frequency, which we obtain from our simulations using decoupled stacks.

Figures 16(a) and 16(b) show results for, respectively, the low-bias regime and the high-bias regime for the case that mutual coupling is mediated by a normal-conducting base segment. The horizontal axes display the difference in the bare frequencies of the two oscillators. For comparison, Figs. 16(c) and 16(d) show the corresponding results for the case of a superconducting base segment representing the minimal model of two mesas located on a common base crystal. In all graphs the left axes display $C(\Delta f)$, while the right axes display $\delta_{\mathrm{f}}$. Figures 16(a) and 16(c) are for the low-bias regime, where the left stack is biased at $i_{\mathrm{left}} = 0.24$. Figures 16(b) and 16(d) are for the high-bias regime, with $i_{\mathrm{left}} = 0.6$. For each pair of bias currents through, respectively, the left stack and the right stack, we performed the simulations five times for different sequences of random numbers. For a given run we used the same random numbers and performed the calculations twice, first for the coupled stacks and afterwards for the decoupled stacks to obtain the bare frequencies.

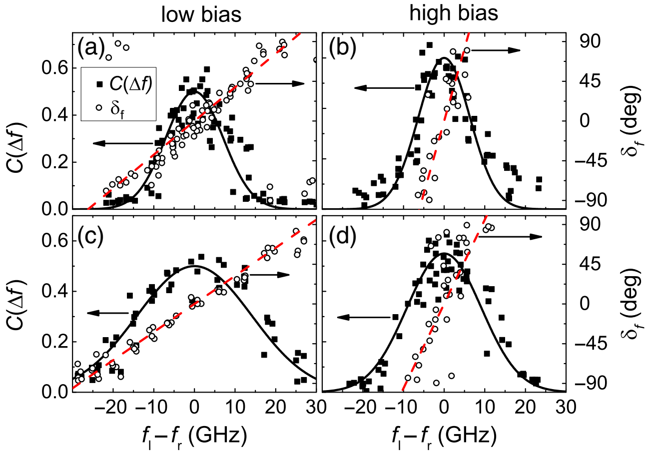

FIG. 16. Correlation functions $C(\Delta f)$ (solid squares, left axes) and the phase $\delta_{\mathrm{f}}$ (open circles, right axes) versus the difference of the bare (uncoupled stacks) frequencies $f_{\mathrm{l}} - f_{\mathrm{r}}$ of, respectively the left stack and the right stack. (a),(b) Normal-conducting common base segment. (c),(d) Fully superconducting base segment. (a),(c) Low-bias regime, with the left stack biased at $i_{\mathrm{left}} = 0.24$. (b),(d) High-bias regime, with the left stack biased at $i_{\mathrm{left}} = 0.6$. The bath temperature is 50 K in all cases.

In each graph we compare $C(\Delta f)$ with a Gaussian, $C(\Delta f) = C_0 e^{-[(f_{\mathrm{b}}-f_{\mathrm{a}})/f_{\mathrm{C}}]^2}$ (solid lines) and for the phase $\delta_{\mathrm{f}}$ we use the linear relation $\delta_{\mathrm{f}} = (f_{\mathrm{b}} - f_{\mathrm{a}})/f_{\delta}$. For $f_{\mathrm{C}}$ we use values of 10 GHz [Fig. 16(a)], 9 GHz [Fig. 16(b)], 20 GHz [Fig. 16(c)], and 13 GHz [Fig. 16(d)], and for $f_{\delta}$ we use 15 GHz [Fig. 16(a)], 3.5 GHz [Fig. 16(b)], 18 GHz [Fig. 16(c)] and 6 GHz [Fig. 16(d)]. These values are at least an order of magnitude larger than the experimental values, which may not be surprising, because in our toy model there is no real physical gap between the two oscillators. On the other hand, Fig. 16 shows that the functional dependences for $C(\Delta f)$ and for $\delta_{\mathrm{f}}$, plus the description as a whole, seem reasonable.

## APPENDIX D: ANALYSIS OF THE LOCK-IN-DETECTED SIGNAL

In the main text the expressions

$$\begin{aligned} S_{\mathrm{X}} &= \frac{P_{\mathrm{X0}}}{P_{\mathrm{Xa}} + P_{\mathrm{Xb}}} C(\Delta f)\cos(\delta_{\mathrm{f}} + \varphi_{\mathrm{X}}) \\ &= S_{\mathrm{X0}} C(\Delta f)\cos(\delta_{\mathrm{f}} + \varphi_{\mathrm{X}}), \end{aligned} \tag{9a}$$

$$S_{\mathrm{Y}} = \frac{P_{\mathrm{Y0}}}{P_{\mathrm{Ya}} + P_{\mathrm{Yb}}} C(\Delta f) \cos(\delta_{\mathrm{f}} + \varphi_{\mathrm{Y}})$$
$$= S_{\mathrm{Y0}} C(\Delta f) \cos(\delta_{\mathrm{f}} + \varphi_{\mathrm{Y}}) \qquad (9b)$$

were used to analyze the lock-in-detected power enhancement of the two interfering terahertz signals generated by stack a and stack b. In the following we derive these expressions and relate them to the parameters of our experimental setup. We relate Eqs. (9a) and (9b) to the local wave fronts emitted by the two stacks. To do so, we first look more precisely at the geometry and the different components of the experiment. After some general considerations, we consider an incoherent signal as it has been used for the hot/cold calibration. Next, we investigate the lock-in signal detected from a coherent beam of a single stack and finally we turn to the case of interfering coherent beams.

### 1. Geometry and general considerations

The overall geometry of the setup and the detection scheme is outlined in the main text; see Fig. 3. An important component is the chopper, which periodically modulates the interfering incoming light fields. Figure 17 sketches projections of various components in the $(x,y)$ plane of the chopper. The view is along the optical axis ("$z$ direction"). The moving chopper is sketched by a series of dark-gray and white rectangles that move to the right with increasing time. This is a simplification, because the actually open and dark sections of the chopper are approximately triangles rotating around an axis that is laterally displaced from the optical axis. In other words, we approximate the action of the chopper by a periodic box function.

For convenience, we introduce a dimensionless time $\tau = \omega_{\mathrm{ch}} t$, i.e., one full dark-bright period corresponds to $2\pi$. We measure spatial coordinates in the unit of $L_{\mathrm{c}}/\pi$, where $L_{\mathrm{c}}$ is the length of the subsequently open (white) and closed (dark gray) parts of the chopper in the $x$ direction. $\xi = \pi x/L_{\mathrm{c}}$ is the dimensionless coordinate in the $x$ direction and $\zeta = \pi y/L_{\mathrm{c}}$ is the dimensionless coordinate in the $y$ direction. Figure 17(a) shows the chopper at a time when the open part of the chopper is centered on the optical axis. For this position we define a static maximum signal area (SA), which is fixed to the optical axis and coincides with the open part of the chopper. In dimensionless units, the (SA) extends from $\xi = -\pi/2$ to $\xi = +\pi/2$. The plot also defines by the on-axis white circle the projection of the first parabolic mirror M1, which extends from $-r$ to $r$ in the $\xi$ direction, with $r \le 2\pi$. M1 defines the relevant area where the emitted radiation is collected. With respect to the full SA, we can simply assume that the amplitude of the emitted radiation is zero outside the area of M1.

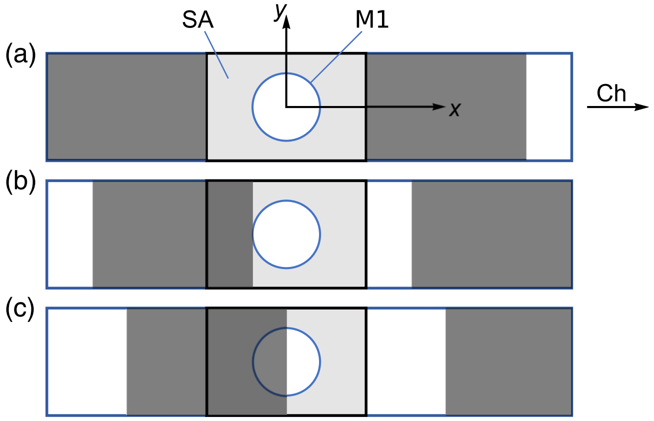

FIG. 17. Projections in the $(x,y)$ plane of the chopper (Ch). The coordinate system is centered at the optical axis. The chopper is sketched by alternating dark-gray and white rectangles of the same size $L_{\mathrm{c}}$ in the $x$ direction. The center circle represents a projection of the first parabolic mirror (M1) onto the chopper plane. SA defines the maximum signal area, defined as the open area when one of the chopper windows is centered on the optical axis. The sketches in (a)–(c) are for three different times and thus chopper positions.

The right edge of the open part of the chopper is ahead in time relative to its center by time difference $\Delta\tau = \pi/2$ and thus reaches a certain spatial location $\xi$ on the SA and M1 at $\tau = \pi/2 - \xi$. Correspondingly, the left edge of the open part of the chopper is behind the center by time difference $\Delta\tau = -\pi/2$ . Figure 17(b) is for time $\tau = \pi/2 - r$, when the left edge has reached M1. Figure 17(c) is for $\tau = \pi/2$, when half of the SA and M1 are shadowed by the chopper.

Figure 18 provides a closer look at the SA and M1 in the presence of the radiation fields emitted by stacks a and b. These fields will be at least partially off-axis and presumably have some overlap region $i$. For the hot/cold calibration using thermal radiation, we assume that M1 is illuminated concentrically.

In all situations we can characterize the incoming signal by a complex light field propagating (approximately) along the optical axis

$$E(\xi,\zeta,t) = E_0(\xi,\zeta) e^{i[\varphi(\xi,\zeta) - \omega t]} \qquad (D1)$$

in the plane of the chopper. Having passed the lens, the phase field $\varphi(\xi,\zeta)$ may vary strongly in an unknown way, as discussed in the main text. Next, the light field described by Eq. (D1) is periodically opened and shadowed by the chopper, leading to a time-modulated light field

$$E(\tau) = E_0(\xi,\zeta) L(\xi,\tau) e^{i[\varphi(\xi,\zeta) - \omega t]}, \qquad (D2)$$

where $L(\xi,\tau)$ parametrizes the size and position of the open part of M1. For an opening chopper window, $L(\xi,\tau)$

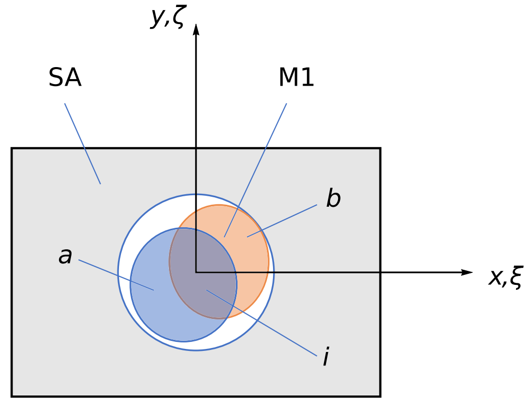

FIG. 18. Maximum signal area SA, projection of the first parabolic mirror M1, and regions illuminated by stacks a and b, plus an overlap area $i$ in the plane of the chopper.

can be written as

$$L(\xi,\tau)=0 \quad \text{for } -\pi \le \tau < \tau_1 = -\pi/2 - r, \quad \text{“M1 not reached yet”}, \tag{D3a}$$

$$L(\xi,\tau)=\Theta(\xi + r) - \Theta(\xi - \tau - \pi/2) \quad \text{for } \tau_1 < \tau < \tau_2 = -\pi/2 + r, \quad \text{“open part of M1 increases”}, \tag{D3b}$$

$$L(\xi,\tau)=\Theta(\xi + r) - \Theta(\xi - r) \quad \text{for } \tau_2 \le \tau \le 0, \text{ “M1 open”}. \tag{D3c}$$

For $0 < \tau \le \pi$, the window closes in reverse order, i.e., we have Eq. (D3c) for $0 \le \tau \le \tau_3 = \pi/2 - r$,

$$L(\xi,\tau)=\Theta(\xi - \tau + \pi/2) - \Theta(\xi - r) \quad \text{for } \tau_3 < \tau < \tau_4 = \pi/2 + r, \tag{D3d}$$

and $L(\xi,\tau)=0$ for $\tau_4 < \tau \le \pi$.

In the expressions above we have ignored the thermal radiation also appearing when the chopper window has closed. This part contributes to the background, which is partially taken care of by the lock-in detection scheme and also by our background-subtraction procedures.

Finally, behind the chopper the (still-propagating-but-now-chopped) light field $E(\tau)$ propagates to the bolometer, building up (unknown) additional phase differences and spatial correlations. Quantitatively we may describe the light field arriving in the bolometer plane by $E_{\mathrm{bol}}(\xi,\zeta,\tau)$, where the electric field at a given point $(\xi,\zeta)$ results from an integration of the form

$$E_{\mathrm{bol}}(\xi,\zeta,\tau,t)=\int d\xi' d\zeta' E(\tau) K(\xi-\xi',\zeta-\zeta'), \tag{D4}$$

with some (complex-valued) spatial correlation function $K(\xi-\xi',\zeta-\zeta')$. $E_{\mathrm{bol}}(\xi,\zeta,\tau,t)$ may be written as

$$E_{\mathrm{bol}}(\xi,\zeta,\tau,t)=E_{\mathrm{bol}\,0}(\xi,\zeta,\tau)e^{i[\varphi_0+\varphi_1(\xi,\zeta,\tau)-\omega t]}, \tag{D5}$$

where we have separated out a global phase $\varphi_0$.

We should then integrate the intensity $E^2_{\mathrm{bol},0}(\xi,\zeta,\tau)$ over the area of the bolometer to yield a final output $P(\tau)$ detected by the lock-in amplifier. Given a proper calibration of the common phase $\varphi_{\mathrm{c}}$ in the lock-in channels X and Y, the lock-in-amplifier outputs, after multiplication by, respectively, $\cos(\tau)$ (channel X) and $\sin(\tau)$ (channel Y) project out the symmetric (X) and antisymmetric (Y) parts of the incoming signal $P(\tau)$.

### 2. Analysis of various light fields

We consider three cases: namely, the case of thermal radiation during the hot/cold calibration measurements, the case of coherent beams of emitters a and b that are mutually unsynchronized, and the case of mutually synchronized emitters a and b.

#### a. Hot/cold calibration

Here, the (thermal) light field is fully incoherent and contains many emission frequencies. The correlation function $K(\xi-\xi',\zeta-\zeta')$ is a $\delta$ function in both $\xi$ and $\zeta$. From Eqs. (D3a)–(D3d) we find that, assuming that all optical components are well aligned with the optical axis, the response $P(\tau)$ is symmetric in $\tau$ if the intensity distribution of the (thermal) light field in the chopper plane was spatially symmetric (i.e., relative to coordinates $\xi$ and $\pi$) on the mirror M1. This (ideally) leads to a finite signal in channel X, and zero signal in channel Y.

#### b. Single oscillator emitting coherently

$E_{\mathrm{bol}}(\xi,\zeta,\tau)$ in general contains interference terms and may have a complicated spatial distribution. The light field $E(\xi,\zeta,t)$ in the chopper plane is not necessarily symmetric with respect to the optical axis (see Fig. 18), and in addition the spatial correlations built up by $K(\xi-\xi',\zeta-\zeta')$ may break original symmetries. Thus, we expect that the lock-in-detected signal $P(\tau)$ does not appear exclusively in channel X, which is the case in our experiments. This can be seen in Fig. 10 showing the four reconstructed curves of the emission powers $P_{\mathrm{a,X}}$, $P_{\mathrm{b,X}}$, $P_{\mathrm{a,Y}}$, and $P_{\mathrm{b,Y}}$ versus the respective emission frequency, where roughly 20% of the signal appears in channel Y. One also notes that for stack a the shape of the curves is quite different in channel X and channel Y. For stack b the differences are less pronounced but still obvious. This rules out that the signal in channel Y is just a low-signal replica of the signal in channel X, which would have happened if the channel-Y signal had a nonzero signal just due to an incorrect setting of the lock-in reference phase.

#### c. Mutually synchronized oscillators a and b

In the plane of the bolometer we have a light field of the form

$$E_{\mathrm{bol}}(\xi,\zeta,\tau,t) = E_{\mathrm{bol\,0,a}}(\xi,\zeta,\tau)e^{i[\varphi_{0\mathrm{a}}+\varphi_{1\mathrm{a}}(\xi,\zeta,\tau)-\omega_{\mathrm{a}}t]} + E_{\mathrm{bol\,0,b}}(\xi,\zeta,\tau)e^{i[\varphi_{0\mathrm{b}}+\varphi_{1\mathrm{b}}(\xi,\zeta,\tau)-\omega_{\mathrm{b}}t]}. \tag{D6}$$

The intensity $E_{\mathrm{bol}}E^*_{\mathrm{bol}}$ is given by

$$E_{\mathrm{bol}}(\xi,\zeta,\tau)E^*_{\mathrm{bol}}(\xi,\zeta,\tau) = E^2_{\mathrm{bol\,0,a}} + E^2_{\mathrm{bol\,0,b}} + 2E_{\mathrm{bol\,0,a}} + E_{\mathrm{bol\,0,b}}\cos[\delta + \Delta\varphi(\xi,\zeta,\tau)], \tag{D7}$$

with the oscillator phase difference $\delta$ (see Appendix C) and the geometric phase difference $\Delta\varphi(\xi,\zeta,\tau) = \varphi_{\mathrm{b}}(\xi,\zeta,\tau) - \varphi_{\mathrm{a}}(\xi,\zeta,\tau)$. Here we omitted the arguments in the amplitude functions for simplicity. The last term on the right-hand side is the interference term. After time-averaging over the fluctuations of $\delta(t)$, one obtains

$$E_{\mathrm{bol}}(\xi,\zeta,\tau,t)E^2_{\mathrm{bol}}(\xi,\zeta,\tau,t) = E^2_{\mathrm{bol\,0,a}} + E^2_{\mathrm{bol\,0,b}} + 2E_{\mathrm{bol\,0,a}}E_{\mathrm{bol\,0,b}}\langle\cos[\delta + \Delta\varphi(\xi,\zeta,\tau)]\rangle, \tag{D8}$$

with $C(\Delta f) = \sqrt{\langle\cos\delta\rangle^2 + \langle\sin\delta\rangle^2}$, $\delta_{\mathrm{f}} = \tan^{-1}(\langle\sin\delta\rangle/\langle\cos\delta\rangle)$, and $\Delta f = f_{\mathrm{b}} - f_{\mathrm{a}}$, given in the main text and discussed in Appendix C, the time-averaged cosine gives

$$\langle\cos[\delta + \Delta\varphi(\xi,\zeta,\tau)]\rangle = C(\Delta f)\cos[\delta_{\mathrm{f}} + \Delta\varphi(\xi,\zeta,\tau)]. \tag{D9}$$

Next, Eq. (D8) should be integrated over the bolometer area, yielding $P(\tau)$, to be multiplied by, respectively, $\cos(\tau)$ and $\sin(\tau)$ and integrated over time. Expanding the cos term in Eq. (D8), we obtain

$$2\sqrt{2}E_{\mathrm{bol\,0,a}}E_{\mathrm{bol\,0,b}}C(\Delta f)\{\cos(\delta_{\mathrm{f}})\cos[\Delta\varphi(\xi,\zeta,\tau)] - \sin(\delta_{\mathrm{f}})\sin[\Delta\varphi(\xi,\zeta,\tau)]\} \tag{D10}$$

and from there after integration over the bolometer area and time, one finds for the lock-in-detected interference term in channel X

$$P_{\mathrm{Xab}} = P_{\mathrm{X,cos}}C(\Delta f)\cos(\delta_{\mathrm{f}}) - P_{\mathrm{X,sin}}C(\Delta f)\sin(\delta_{\mathrm{f}}), \tag{D11}$$

which can be reformulated as

$$P_{\mathrm{Xab}} = P_{\mathrm{X,0}}C(\Delta f)\cos(\delta_{\mathrm{f}} + \varphi_{\mathrm{X}}),\ \text{with}\quad P_{\mathrm{X,0}} = \sqrt{P^2_{\mathrm{X,cos}} + P^2_{\mathrm{X,sin}}}\ \text{and}\ \varphi_{\mathrm{X}} = \tan^{-1}\left(\frac{P_{\mathrm{X,sin}}}{P_{\mathrm{X,cos}}}\right). \tag{D12}$$

Similarly, we obtain for channel Y

$$P_{\mathrm{Yab}} = P_{\mathrm{Y,0}}C(\Delta f)\cos(\delta_{\mathrm{f}} + \varphi_{\mathrm{Y}}),\ \text{with}\quad P_{\mathrm{Y,0}} = \sqrt{P^2_{\mathrm{Y,cos}} + P^2_{\mathrm{Y,sin}}}\ \text{and}\ \varphi_{\mathrm{Y}} = \tan^{-1}\left(\frac{P_{\mathrm{Y,sin}}}{P_{\mathrm{Y,cos}}}\right). \tag{D13}$$

The overall response in the two channels can be written as

$$P_{\mathrm{X}} = P_{\mathrm{X,a}} + P_{\mathrm{X,\,b}} + P_{\mathrm{X,0}}C(\Delta f)\cos(\delta_{\mathrm{f}} + \varphi_{\mathrm{X}})\quad\text{(channel X)}, \tag{D14}$$

$$P_{\mathrm{Y}} = P_{\mathrm{Y,a}} + P_{\mathrm{Y,\,b}} + P_{\mathrm{Y,0}}C(\Delta f)\cos(\delta_{\mathrm{f}} + \varphi_{\mathrm{Y}})\quad\text{(channel Y)}. \tag{D15}$$

After determining the background relative to the interference term, as outlined in Appendix B, and division by the background one obtains

$$S_{\mathrm{X}} = \frac{P_{\mathrm{X,0}}}{P_{\mathrm{X,a}} + P_{\mathrm{X,b}}}C(\Delta f)\cos(\delta_{\mathrm{f}} + \varphi_{\mathrm{X}}) = S_{\mathrm{X,0}}C(\Delta f)\cos(\delta_{\mathrm{f}} + \varphi_{\mathrm{X}})\quad\text{(channel X)}, \tag{D16}$$

$$S_{\mathrm{Y}} = \frac{P_{\mathrm{Y,0}}}{P_{\mathrm{Y,a}} + P_{\mathrm{Y,b}}}C(\Delta f)\cos(\delta_{\mathrm{f}} + \varphi_{\mathrm{Y}}) = S_{\mathrm{Y,0}}C(\Delta f)\cos(\delta_{\mathrm{f}} + \varphi_{\mathrm{Y}})\quad\text{(channel Y)}, \tag{D17}$$

which are the functions used in the main text.

$P_{\mathrm{X,a}}$, $P_{\mathrm{X,b}}$, $P_{\mathrm{Y,a}}$, and $P_{\mathrm{Y,b}}$ can be obtained from the experimental data via analysis of the background as outlined in Appendix B. $P_{\mathrm{X,0}}$ and $P_{\mathrm{Y,0}}$ are not accessible independently of $C(\Delta f = 0) = C_0$. However, we note that $P_{\mathrm{X,0}}$ and $P_{\mathrm{Y,0}}$ result from spatial integrations over the terms $E_{\mathrm{bol\,0,a}}E_{\mathrm{bol\,0,b}}\cos[\Delta\varphi(\xi,\zeta)]$ and $E_{\mathrm{bol\,0,a}}E_{\mathrm{bol\,0,b}}\sin[\Delta\varphi(\xi,\zeta)]$ in Eq. (D10). They can be very small if the cosine and sine functions change sign often over the bolometer area. As a consequence, small values of the products $S_{\mathrm{X,0}}C_0$ and $S_{\mathrm{Y,0}}C_0$ do not imply that the maximum value of $C_0$ is small. Thus, we can get information on the shape and the width of $C(\Delta f)$ but not on its magnitude $C_0$. More details are given in the main text.

[1] B. Ferguson and X. C. Zhang, Materials for terahertz science and technology, Nat. Mater. **1**, 26 (2002).

[2] M. Tonouchi, Cutting-edge terahertz technology, Nat. Photonics **1**, 97 (2007).

[3] B. S. Williams, Terahertz quantum-cascade lasers, Nat. Photonics **1**, 517 (2007).

[4] M. Feiginov, H. Kanaya, S. Suzuki, and M. Asada, Operation of resonant-tunneling diodes with strong back injection from the collector at frequencies up to 1.46 THz, Appl. Phys. Lett. **104**, 243509 (2014).

[5] R. Kleiner, F. Steinmeyer, G. Kunkel, and P. Müller, Intrinsic Josephson effect in $Bi_2Sr_2CaCu_2O_8$ single crystals, Phys. Rev. Lett. **68**, 2394 (1992).

[6] L. Ozyuzer, A. E. Koshelev, C. Kurter, N. Gopalsami, Q. Li, M. Tachiki, K. Kadowaki, T. Yamamoto, H. Minami, H. Yamaguchi, T. Tachiki, K. E. Gray, W.-K. Kwok, and U. Welp, Emission of coherent THz radiation from superconductors, Science **318**, 1291 (2007).

[7] H. B. Wang, S. Guénon, J. Yuan, A. Iishi, S. Arisawa, T. Hatano, T. Yamashita, D. Koelle, and R. Kleiner, Hot spots and waves in $Bi_2Sr_2CaCu_2O_8$ intrinsic Josephson junction stacks: A study by low temperature scanning laser microscopy, Phys. Rev. Lett. **102**, 017006 (2009).

[8] H. Minami, I. Kakeya, H. Yamaguchi, T. Yamamoto, and K. Kadowaki, Characteristics of terahertz radiation emitted from the intrinsic Josephson junctions in high-$T_c$ superconductor $Bi_2Sr_2CaCu_2O_{8+\delta}$, Appl. Phys. Lett. **95**, 232511 (2009).

[9] C. Kurter, L. Ozyuzer, T. Proslier, J. F. Zasadzinski, D. G. Hinks, and K. E. Gray, Counterintuitive consequence of heating in strongly-driven intrinsic junctions of $Bi_2Sr_2CaCu_2O_{8+\delta}$ mesas, Phys. Rev. B **81**, 224518 (2010).

[10] H. B. Wang, S. Guénon, B. Gross, J. Yuan, Z. G. Jiang, Y. Y. Zhong, M. Grünzweig, A. Iishi, P. H. Wu, T. Hatano, D. Koelle, and R. Kleiner, Coherent terahertz emission of intrinsic Josephson junction stacks in the hot spot regime, Phys. Rev. Lett. **105**, 057002 (2010).

[11] M. Tsujimoto, K. Yamaki, K. Deguchi, T. Yamamoto, T. Kashiwagi, H. Minami, M. Tachiki, K. Kadowaki, and R. A. Klemm, Geometrical resonance conditions for THz radiation from the intrinsic Josephson junctions in $Bi_2Sr_2CaCu_2O_{8+\delta}$, Phys. Rev. Lett. **105**, 037005 (2010).

[12] N. Orita, H. Minami, T. Koike, T. Yamamoto, and K. Kadowaki, Synchronized operation of two serially connected Bi2212 THz emitters, Physica C **470**, S786 (2010).

[13] S. Guénon, M. Grünzweig, B. Gross, J. Yuan, Z. G. Jiang, Y. Y. Zhong, M. Y. Li, A. Iishi, P. H. Wu, T. Hatano, R. G. Mints, E. Goldobin, D. Koelle, H. B. Wang, and R. Kleiner, Interaction of hot spots and terahertz waves in $Bi_2Sr_2CaCu_2O_8$ intrinsic Josephson junction stacks of various geometry, Phys. Rev. B **82**, 214506 (2010).

[14] T. M. Benseman, A. E. Koshelev, K. E. Gray, W.-K. Kwok, U. Welp, K. Kadowaki, M. Tachiki, and T. Yamamoto, Tunable terahertz emission from $Bi_2Sr_2CaCu_2O_{8+\delta}$ mesa devices, Phys. Rev. B **84**, 064523 (2011).

[15] K. Yamaki, M. Tsujimoto, T. Yamamoto, A. Furukawa, T. Kashiwagi, H. Minami, and K. Kadowaki, High-power terahertz electromagnetic wave emission from high-$T_c$ superconducting $Bi_2Sr_2CaCu_2O_{8+\delta}$ mesa structures, Opt. Express **19**, 3193 (2011).

[16] M. Y. Li, J. Yuan, N. Kinev, J. Li, B. Gross, S. Guénon, A. Ishii, K. Hirata, T. Hatano, D. Koelle, R. Kleiner, V. P. Koshelets, H. B. Wang, and P. H. Wu, Linewidth dependence of coherent terahertz emission from $Bi_2Sr_2CaCu_2O_8$ intrinsic Josephson junction stacks in the hot-spot regime, Phys. Rev. B **86**, 060505(R) (2012).

[17] I. Kakeya, Y. Omukai, T. Yamamoto, K. Kadowaki, and M. Suzuki, Effect of thermal inhomogeneity for terahertz radiation from intrinsic Josephson junction stacks of $Bi_2Sr_2CaCu_2O_{8+\delta}$, Appl. Phys. Lett. **100**, 242603 (2012).

[18] D. Y. An, *et al.*, Terahertz emission and detection both based on high-$T_c$ superconductors: Towards an integrated receiver, Appl. Phys. Lett. **102**, 092601 (2013).

[19] T. M. Benseman, A. E. Koshelev, W.-K. Kwok, U. Welp, V. K. Vlasko-Vlasov, K. Kadowaki, H. Minami, and C. Watanabe, Direct imaging of hot spots in $Bi_2Sr_2CaCu_2O_{8+\delta}$ mesa terahertz sources, J. Appl. Phys. **113**, 133902 (2013).

[20] T. M. Benseman, K. E. Gray, A. E. Koshelev, W.-K. Kwok, U. Welp, H. Minami, K. Kadowaki, and T. Yamamoto, Powerful terahertz emission from $Bi_2Sr_2CaCu_2O_{8+\delta}$ mesa arrays, Appl. Phys. Lett. **103**, 022602 (2013).

[21] H. Minami, C. Watanabe, K. Sato, S. Sekimoto, T. Yamamoto, T. Kashiwagi, R. A. Klemm, and K. Kadowaki, Local SiC photoluminescence evidence of hot spot formation and sub-THz coherent emission from a rectangular $Bi_2Sr_2CaCu_2O_{8+\delta}$ mesa, Phys. Rev. B **89**, 054503 (2014).

[22] M. Tsujimoto, H. Kambara, Y. Maeda, Y. Yoshioka, Y. Nakagawa, and I. Kakeya, Dynamic control of temperature distributions in stacks of intrinsic Josephson junctions in $Bi_2Sr_2CaCu_2O_{8+\delta}$ for intense terahertz radiation, Phys. Rev. Appl. **2**, 044016 (2014).

[23] M. Ji, J. Yuan, B. Gross, F. Rudau, D. Y. An, M. Y. Li, X. J. Zhou, Y. Huang, H. C. Sun, Q. Zhu, J. Li, N. Kinev, T. Hatano, V. P. Koshelets, D. Koelle, R. Kleiner, W. W. Xu, B. B. Jin, H. B. Wang, and P. H. Wu, $Bi_2Sr_2CaCu_2O_8$ intrinsic Josephson junction stacks with improved cooling: Coherent emission above 1 THz, Appl. Phys. Lett. **105**, 122602 (2014).

[24] T. Kashiwagi, K. Sakamoto, H. Kubo, Y. Shibano, T. Enomoto, T. Kitamura, K. Asanuma, T. Yasui, C. Watanabe, K. Nakade, Y. Saiwai, T. Katsuragawa, M. Tsujimoto, R. Yoshizaki, T. Yamamoto, H. Minami, R. A. Klemm, and K. Kadowaki, A high-$T_c$ intrinsic Josephson junction emitter tunable from 0.5 to 2.4 terahertz, Appl. Phys. Lett. **107**, 082601 (2015).

[25] X. J. Zhou, J. Yuan, H. Wu, Z. S. Gao, M. Ji, D. Y. An, Y. Huang, F. Rudau, R. Wieland, B. Gross, N. Kinev, J. Li, A. Ishii, T. Hatano, V. P. Koshelets, D. Koelle, R. Kleiner, H. B. Wang, and P. H. Wu, Tuning the terahertz emission power of an intrinsic Josephson-junction stack with a focused laser beam, Phys. Rev. Appl. **3**, 044012 (2015).

[26] X. J. Zhou, Q. Zhu, M. Ji, D. Y. An, L. Y. Hao, H. C. Sun, S. Ishida, F. Rudau, R. Wieland, J. Li, D. Koelle, H. Eisaki,

Y. Yoshida, T. Hatano, R. Kleiner, H. B. Wang, and P. H. Wu, Three-terminal stand-alone superconducting terahertz emitter, Appl. Phys. Lett. **107**, 122602 (2015).

[27] C. Watanabe, H. Minami, T. Kitamura, K. Asanuma, K. Nakade, T. Yasui, Y. Saiwai, Y. Shibano, T. Yamamoto, T. Kashiwagi, R. A. Klemm, and K. Kadowaki, Influence of the local heating position on the terahertz emission power from high-$T_c$ superconducting $Bi_2Sr_2CaCu_2O_{8+\delta}$ mesas, Appl. Phys. Lett. **106**, 042603 (2015).

[28] T. Kashiwagi, T. Yamamoto, T. Kitamura, K. Asanuma, C. Watanabe, K. Nakade, T. Yasui, Y. Saiwai, Y. Shibano, H. Kubo, K. Sakamoto, T. Katsuragawa, M. Tsujimoto, K. Delfanazari, R. Yoshizaki, H. Minami, R. A. Klemm, and K. Kadowaki, Generation of electromagnetic waves from 0.3 to 1.6 terahertz with a high-$T_c$ superconducting $Bi_2Sr_2CaCu_2O_{8+\delta}$ intrinsic Josephson junction emitter, Appl. Phys. Lett. **106**, 092601 (2015).

[29] T. Kashiwagi, *et al.*, Efficient fabrication of intrinsic-Josephson-junction terahertz oscillators with greatly reduced self-heating effects, Phys. Rev. Appl. **4**, 054018 (2015).

[30] B. Gross, F. Rudau, N. Kinev, M. Tsujimoto, J. Yuan, Y. Huang, M. Ji, X. J. Zhou, D. Y. An, A. Iishi, P. H. Wu, T. Hatano, D. Koelle, H. B. Wang, V. P. Koshelets, and R. Kleiner, Electrothermal behavior and terahertz emission properties of a planar array of two $Bi_2Sr_2CaCu_2O_{8+\delta}$ intrinsic Josephson junction stacks, Supercond. Sci. Technol. **28**, 055004 (2015).

[31] T. M. Benseman, A. E. Koshelev, V. Vlasko-Vlasov, Y. Hao, W.-K. Kwok, U. Welp, C. Keiser, B. Gross, M. Lange, D. Kölle, R. Kleiner, H. Minami, C. Watanabe, and K. Kadowaki, Current filamentation in large $Bi_2Sr_2CaCu_2O_{8+\delta}$ mesa devices observed via luminescent and scanning laser thermal microscopy, Phys. Rev. Appl. **3**, 044017 (2015).

[32] K. Nakade, T. Kashiwagi, Y. Saiwai, H. Minami, T. Yamamoto, R. A. Klemm, and K. Kadowaki, Applications using high-$T_c$ superconducting terahertz emitters, Sci. Rep. **6**, 23178 (2016).

[33] M. Tsujimoto, I. Kakeya, T. Kashiwagi, H. Minami, and K. Kadowaki, Cavity mode identification for coherent terahertz emission from high-$T_c$ superconductors, Opt. Express **24**, 4591 (2016).

[34] H. C. Sun, *et al.*, Terahertz spectroscopy of dilute gases using $Bi_2Sr_2CaCu_2O_{8+\delta}$ intrinsic Josephson-junction stacks, Phys. Rev. Appl. **8**, 054005 (2017).

[35] A. Elarabi, Y. Yoshioka, M. Tsujimoto, and I. Kakeya, Monolithic superconducting emitter of tunable circularly polarized terahertz radiation, Phys. Rev. Appl. **8**, 064034 (2017).

[36] E. A. Borodianskyi and V. M. Krasnov, Josephson emission with frequency span 1–11 THz from small $Bi_2Sr_2CaCu_2O_{8+\delta}$ mesa structures, Nat. Commun. **8**, 1742 (2017).

[37] T. Kashiwagi, T. Yuasa, Y. Tanabe, T. Imai, G. Kuwano, R. Ota, K. Nakamura, Y. Ono, Y. Kaneko, M. Tsujimoto, H. Minami, T. Yamamoto, R. A. Klemm, and K. Kadowaki, Improved excitation mode selectivity of high-$T_c$ superconducting terahertz emitters, J. Appl. Phys. **124**, 033901 (2018).

[38] H. Minami, Y. Ono, K. Murayama, Y. Tanabe, K. Nakamura, S. Kusunose, T. Kashiwagi, M. Tsujimoto, and K. Kadowaki, Power enhancement of the high-$T_c$ superconducting terahertz emitter with a modified device structure, J. Phys.: Conf. Ser. **1293**, 012056 (2019).

[39] H. Zhang, *et al.*, Resonant cavity modes in $Bi_2Sr_2CaCu_2O_{8+x}$ intrinsic Josephson junction stacks, Phys. Rev. Appl. **11**, 044004 (2019).

[40] T. M. Benseman, A. E. Koshelev, V. Vlasko-Vlasov, Y. Hao, U. Welp, W.-K. Kwok, B. Gross, M. Lange, D. Koelle, R. Kleiner, H. Minami, M. Tsujimoto, and K. Kadowaki, Observation of a two-mode resonant state in a $Bi_2Sr_2CaCu_2O_{8+\delta}$ mesa device for terahertz emission, Phys. Rev. B **100**, 144503 (2019).

[41] G. Kuwano, M. Tsujimoto, Y. Kaneko, T. Imai, Y. Ono, S. Nakagawa, S. Kusunose, H. Minami, T. Kashiwagi, K. Kadowaki, Y. Simsek, U. Welp, and W.-K. Kwok, Mesa-sidewall effect on coherent terahertz radiation via spontaneous synchronization of intrinsic Josephson junctions in $Bi_2Sr_2CaCu_2O_{8+\delta}$, Phys. Rev. Appl. **13**, 014035 (2020).

[42] M. Tsujimoto, S. Fujita, G. Kuwano, K. Maeda, A. Elarabi, J. Hawecker, J. Tignon, J. Mangeney, S. S. Dhillon, and I. Kakeya, Mutually synchronized macroscopic Josephson oscillations demonstrated by polarization analysis of superconducting terahertz emitters, Phys. Rev. Appl. **13**, 051001 (2020).

[43] Y. Ono, H. Minami, G. Kuwano, T. Kashiwagi, M. Tsujimoto, K. Kadowaki, and R. A. Klemm, Superconducting emitter powered at 1.5 terahertz by an external resonator, Phys. Rev. Appl. **13**, 064026 (2020).

[44] R. Cattaneo, E. A. Borodianskyi, A. A. Kalenyuk, and V. M. Krasnov, Superconducting terahertz sources with 12% power efficiency, Phys. Rev. Appl. **16**, L061001 (2021).

[45] M. Tsujimoto, Y. Kaneko, G. Kuwano, K. Nagayama, T. Imai, Y. Ono, S. Kusunose, T. Kashiwagi, H. Minami, K. Kadowaki, Y. Simsek, U. Welp, and W.-K. Kwok, Design and characterization of microstrip patch antennas for high-$T_c$ superconducting terahertz emitters, Opt. Express **29**, 16980 (2021).

[46] G. Kuwano, M. Tsujimoto, Y. Kaneko, K. Nagayama, T. Imai, Y. Ono, S. Kusunose, T. Yuhara, H. Minami, T. Kashiwagi, and K. Kadowaki, Experimental validation of a microstrip antenna model for high-$T_c$ superconducting terahertz emitters, J. Appl. Phys. **129**, 223905 (2021).

[47] T. Kashiwagi, T. Yuasa, G. Kuwano, T. Yamamoto, M. Tsujimoto, H. Minami, and K. Kadowaki, Study of radiation characteristics of intrinsic Josephson junction terahertz emitters with different thickness of $Bi_2Sr_2CaCu_2O_{8+\delta}$ crystals, Materials **14**, 1135 (2021).

[48] H. Sun, S. Chen, Y.-L. Wang, G. Sun, J. Chen, T. Hatano, V. P. Koshelets, D. Koelle, R. Kleiner, H. Wang, and P. Wu, Compact high-$T_c$ superconducting terahertz emitter with tunable frequency from 0.15 to 1 THz, Appl. Sci. **13**, 3469 (2023).

[49] K. J. Kihlstrom, K. C. Reddy, S. Elghazoly, T. E. Sharma, A. E. Koshelev, U. Welp, Y. Hao, R. Divan, M. Tsujimoto, K. Kadowaki, W.-K. Kwok, and T. M. Benseman, Powerful terahertz emission from a $Bi_2Sr_2CaCu_2O_{8+\delta}$ mesa operating above 77 K, Phys. Rev. Appl. **19**, 034055 (2023).

[50] M. Miyamoto, R. Kobayashi, G. Kuwano, M. Tsujimoto, and I. Kakeya, Wide-band frequency modulation of a terahertz intrinsic Josephson junction emitter of a cuprate superconductor, Nat. Photonics **18**, 267 (2024).

[51] A. Elarabi, Y. Saito, H. Asai, R. Kobayashi, K. Hayama, K. Maeda, S. Fujita, Y. Yoshioka, Y. Takano, M. Tsujimoto, and I. Kakeya, Polarized terahertz electromagnetic-wave radiation from cuprate superconductor Bi2212 mesa structures, Jap. J. Appl. Phys. **63**, 020801 (2024).

[52] L. N. Bulaevskii and A. E. Koshelev, Radiation due to Josephson oscillations in layered superconductors, Phys. Rev. Lett. **99**, 057002 (2007).

[53] S. Z. Lin and X. Hu, Possible dynamic states in inductively coupled intrinsic Josephson junctions of layered high-$T_c$ superconductors, Phys. Rev. Lett. **100**, 247006 (2008).

[54] X. Hu and S. Z. Lin, Three-dimensional phase-kink state in a thick stack of Josephson junctions and terahertz radiation, Phys. Rev. B **78**, 134510 (2008).

[55] R. A. Klemm and K. Kadowaki, Output from a Josephson stimulated terahertz amplified radiation emitter, J. Phys. Cond. Mat. **22**, 375701 (2010).

[56] V. M. Krasnov, Coherent flux-flow emission from stacked Josephson junctions: Nonlocal radiative boundary conditions and the role of geometrical resonances, Phys. Rev. B **82**, 134524 (2010).

[57] A. E. Koshelev, Stability of dynamic coherent states in intrinsic Josephson-junction stacks near internal cavity resonance, Phys. Rev. B **82**, 174512 (2010).

[58] K. Kadowaki, M. Tsujimoto, K. Yamaki, T. Yamamoto, T. Kashiwagi, H. Minami, M. Tachiki, and R. A. Klemm, Evidence for a dual-source mechanism of terahertz radiation from rectangular mesas of single crystalline $Bi_2Sr_2CaCu_2O_{8+\delta}$ intrinsic Josephson junctions, J. Phys. Soc. Jpn **79**, 023703 (2010).

[59] A. Yurgens, Temperature distribution in a large $Bi_2Sr_2CaCu_2O_{8+\delta}$ mesa, Phys. Rev. B **83**, 184501 (2011).

[60] S. Z. Lin and X. Hu, In-plane dissipation as a possible synchronization mechanism for terahertz radiation from intrinsic Josephson junctions of layered superconductors, Phys. Rev. B **86**, 054506 (2012).

[61] H. Asai, M. Tachiki, and K. Kadowaki, Three-dimensional numerical analysis of terahertz radiation emitted from intrinsic Josephson junctions with hot spots, Phys. Rev. B **85**, 064521 (2012).

[62] H. Asai, M. Tachiki, and K. Kadowaki, Proposal of terahertz patch antenna fed by intrinsic Josephson junctions, Appl. Phys. Lett. **101**, 112602 (2012).

[63] B. Gross, S. Guénon, J. Yuan, M. Y. Li, J. Li, A. Ishii, R. G. Mints, T. Hatano, P. H. Wu, D. Koelle, H. B. Wang, and R. Kleiner, Hot-spot formation in stacks of intrinsic Josephson junctions in $Bi_2Sr_2CaCu_2O_8$, Phys. Rev. B **86**, 094524 (2012).

[64] S.-Z. Lin and A. E. Koshelev, Synchronization of Josephson oscillations in a mesa array of $Bi_2Sr_2CaCu_2O_{8+\delta}$ through the Josephson plasma waves in the base crystal, Physica C **491**, 24 (2013).

[65] S. Z. Lin, Mutual synchronization of two stacks of intrinsic Josephson junctions in cuprate superconductors, J. Appl. Phys. **115**, 173901 (2014).

[66] F. Rudau, M. Tsujimoto, B. Gross, T. E. Judd, R. Wieland, E. Goldobin, N. Kinev, J. Yuan, Y. Huang, M. Ji, X. J. Zhou, D. Y. An, A. Ishii, R. G. Mints, P. H. Wu, T. Hatano, H. B. Wang, V. P. Koshelets, D. Koelle, and R. Kleiner, Thermal and electromagnetic properties of $Bi_2Sr_2CaCu_2O_8$ intrinsic Josephson junction stacks studied via one-dimensional coupled sine-Gordon equations, Phys. Rev. B **91**, 104513 (2015).

[67] F. Rudau, R. Wieland, J. Langer, X. J. Zhou, M. Ji, N. Kinev, L. Y. Hao, Y. Huang, J. Li, P. H. Wu, T. Hatano, V. P. Koshelets, H. B. Wang, D. Koelle, and R. Kleiner, Three-dimensional simulations of the electrothermal and terahertz emission properties of $Bi_2Sr_2CaCu_2O_8$ intrinsic Josephson junction stacks, Phys. Rev. Appl. **5**, 044017 (2016).

[68] H. Asai and S. Kawabata, Control of circularly polarized THz wave from intrinsic Josephson junctions by local heating, Appl. Phys. Lett. **110**, 132601 (2017).

[69] D. P. Cerkoney, C. Reid, C. M. Doty, A. Gramajo, T. D. Campbell, M. A. Morales, K. Delfanazari, M. Tsujimoto, T. Kashiwagi, T. Yamamoto, C. Watanabe, H. Minami, K. Kadowaki, and R. A. Klemm, Cavity mode enhancement of terahertz emission from equilateral triangular microstrip antennas of the high-$T_c$ superconductor $Bi_2Sr_2CaCu_2O_{8+\delta}$, J. Phys.: Condens. Matter **29**, 015601 (2017).

[70] R. A. Klemm, A. E. Davis, Q. X. Wang, T. Yamamoto, D. P. Cerkoney, C. Reid, M. L. Koopman, H. Minami, T. Kashiwagi, J. R. Rain, C. M. Doty, M. A. Sedlack, M. A. Morales, C. Watanabe, M. Tsujimoto, K. Delfanazari, and K. Kadowaki, Terahertz emission from the intrinsic Josephson junctions of high-symmetry thermally-managed $Bi_2Sr_2CaCu_2O_{8+\delta}$ microstrip antennas, IOP Conf. Ser.: Mater. Sci. Eng. **279**, 012017 (2017).

[71] A. Sheikhzada and A. Gurevich, Instability of flux flow and production of vortex-antivortex pairs by current-driven Josephson vortices in layered superconductors, Phys. Rev. B **99**, 214512 (2019).

[72] J. R. Rain, P. Y. Cai, A. Baekey, M. A. Reinhard, R. I. Vasquez, A. C. Silverman, C. L. Cain, and R. A. Klemm, Wave functions for high-symmetry, thin microstrip antennas, and two-dimensional quantum boxes, Phys. Rev. A **104**, 062205 (2021).

[73] M. M. Krasnov, N. D. Novikova, R. Cattaneo, A. A. Kalenyuk, and V. M. Krasnov, Design aspects of $Bi_2Sr_2CaCu_2O_{8+\delta}$ THz sources: Optimization of thermal and radiative properties, Beilstein J. Nanotechnol. **12**, 1392 (2021).

[74] S. Kalhor, M. Ghanaatshoar, H. J. Joyce, D. A. Ritchie, K. Kadowaki, and K. Delfanazari, Millimeter-wave-to-terahertz superconducting plasmonic waveguides for integrated nanophotonics at cryogenic temperatures, Materials **14**, 4291 (2021).

[75] R. Kobayashi, K. Hayama, and I. Kakeya, Circuit models of simultaneously biased intrinsic Josephson junction stacks for terahertz radiations in high-bias regime, Appl. Phys. Express **15**, 093002 (2022).

[76] R. Kobayashi, K. Hayama, S. Fujita, M. Tsujimoto, and I. Kakeya, Spontaneous frequency shift and phase delay of coupled terahertz radiation mediated by the Josephson

plasmon in a cuprate superconductor, Phys. Rev. Appl. **17,** 054043 (2022).

[77] U. Welp, K. Kadowaki, and R. Kleiner, Superconducting emitters of THz radiation, Nat. Photonics **7,** 702 (2013).

[78] I. Kakeya and H. B. Wang, Terahertz-wave emission from Bi2212 intrinsic Josephson junctions: A review on recent progress, Supercond. Sci. Technol. **29,** 073001 (2016).

[79] T. Kashiwagi, H. Kubo, K. Sakamoto, T. Yuasa, Y. Tanabe, C. Watanabe, T. Tanaka, Y. Komori, R. Ota, G. Kuwano, K. Nakamura, T. Katsuragawa, M. Tsujimoto, T. Yamamoto, R. Yoshizaki, H. Minami, K. Kadowaki, and R. A. Klemm, The present status of high-$T_c$ superconducting terahertz emitters, Supercond. Sci. Technol. **30,** 074008 (2017).

[80] R. Kleiner and H. B. Wang, Terahertz emission from $Bi_2Sr_2CaCu_2O_{8+x}$ intrinsic Josephson junction stacks, J. Appl. Phys. **126,** 171101 (2019).

[81] K. Delfanazari, R. A. Klemm, H. J. Joyce, D. A. Ritchie, and K. Kadowaki, Integrated, portable, tunable, and coherent terahertz sources and sensitive detectors based on layered superconductors, Proc. IEEE **108,** 721 (2020).

[82] V. M. Krasnov, A distributed active patch antenna model of a Josephson oscillator, Beilstein J. Nanotechnol. **14,** 151 (2023).

[83] S. P. Benz and C. J. Burroughs, Coherent emission from two-dimensional Josephson junction arrays, Appl. Phys. Lett. **58,** 2162 (1991).

[84] P. Barbara, A. B. Cawthorne, S. V. Shitov, and C. J. Lobb, Stimulated emission and amplification in Josephson junction arrays, Phys. Rev. Lett. **82,** 1963 (1999).

[85] M. Darula, T. Doderer, and S. Beuven, Millimetre and sub-mm wavelength radiation sources based on discrete Josephson junction arrays, Supercond. Sci. Technol. **12,** R1 (1999).

[86] F. Song, F. Müller, R. Behr, and A. M. Klushin, Coherent emission from large arrays of discrete Josephson junctions, Appl. Phys. Lett. **95,** 172501 (2009).

[87] M. A. Galin, F. Rudau, E. A. Borodianskyi, V. V. Kurin, D. Koelle, R. Kleiner, V. M. Krasnov, and A. M. Klushin, Direct visualization of phase-locking of large Josephson junction arrays by surface electromagnetic waves, Phys. Rev. Appl. **14,** 024051 (2020).

[88] M. A. Galin, V. M. Krasnov, I. A. Shereshevsky, N. K. Vdovicheva, and V. V. Kurin, Coherent amplification of radiation from two phase-locked Josephson junction arrays, Beilstein J. Nanotechnol. **13,** 1445 (2022).

[89] V. P. Koshelets, N. V. Kinev, A. B. Ermakov, R. Wieland, E. Dorsch, O. Kizilaslan, D. Koelle, R. Kleiner, and H. B. Wang, in *30th International Symposium on Space THz Technology (ISSTT2019)* (Gothenburg, 2019), pp. 128–132.

[90] V. P. Koshelets, P. N. Dmitriev, M. I. Faley, L. V. Filippenko, K. V. Kalashnikov, N. V. Kinev, O. S. Kiselev, A. A. Artanov, K. I. Rudakov, A. de Lange, G. de Lange, V. L. Vaks, M. Y. Li, and H. B. Wang, Superconducting integrated terahertz spectrometers, IEEE Trans. Terahertz Sci. Technol. **5,** 687 (2015).

[91] T. Watanabe, T. Fujii, and A. Matsuda, Anisotropic resistivities of precisely oxygen controlled single-crystal $Bi_2Sr_2CaCu_2O_{8+\delta}$: Systematic study on “spin gap” effect, Phys. Rev. Lett. **79,** 2113 (1997).

[92] N. Chopra and J. Lloyd-Hughes, Optimum optical designs for diffraction-limited terahertz spectroscopy and imaging systems using off-axis parabolic mirrors, J. Infrared Millimeter Terahertz Waves **44,** 981 (2023).

[93] Y. Kuramoto, Self-entrainment of a population of coupled non-linear oscillators, Lect. Notes Phys. **39,** 420 (1975).

[94] K. Wiesenfeld, P. Colet, and S. H. Strogatz, Synchronization transitions in a disordered Josephson series array, Phys. Rev. Lett. **76,** 404 (1996).